Original Article

Investigation of particle deposition on a micropatterned surface as an energy-efficient air cleaning technique in ventilation ducting systems

Haolun Xu [a], Sau Chung Fu [b], Ka Chung Chan [b] and Christopher Y.H. Chao [b]

[a] Department of Mechanical and Aerospace Engineering, The Hong Kong University of Science and Technology, Clear Water Bay, Hong Kong

[b] Department of Mechanical Engineering, The University of Hong Kong, Pok Fu Lam, Hong Kong

Running Head: Submicron Particle Deposition on a Micropattern

Address all correspondence to:

Christopher Y. H. Chao

Department of Mechanical Engineering

The University of Hong Kong

Pok Fu Lam,

Hong Kong, China

Email: cyhchao@hku.hk

Phone: 852-3917-2800

Investigation of particle deposition on a micropatterned surface as an energy-efficient air cleaning technique in ventilation ducting systems

Haolun Xu [a], Sau Chung Fu [b], Ka Chung Chan [b] and Christopher Y.H. Chao [b*]

[a] *Department of Mechanical and Aerospace Engineering, The Hong Kong University of Science and Technology, Clear Water Bay, Hong Kong*

[b] *Department of Mechanical Engineering, The University of Hong Kong, Pok Fu Lam, Hong Kong*

[*] *Corresponding author: cyhchao@hku.hk*

Abstract

Building ventilation ducting systems play a core role in controlling indoor air quality by recirculating the indoor air and mixing with ambient air. As particles are a main pollutant, it is crucial they are removed from both the recirculating indoor air and ambient air. The ventilation system can serve as an air cleaning system itself either through the filtration system or integrating other means, while at the same time, attention to energy consumption is needed. The high-efficiency fibrous filters in a conventional filtration system not only cause high-pressure drops that consume fan energy but also add to the high operation cost. This paper proposes an air cleaning technique, aimed at submicron particles, by means of installing patterned surfaces on the walls of ventilation ducts, which can be easily cleaned by water and reused. The effect of patterned surfaces on particle deposition was studied numerically. In the numerical simulation, the Reynolds stress turbulent model was correlated at the near-wall regions by turbulent velocity fluctuation at the normal direction. Particle trajectory was solved by using Lagrangian particle tracking. The numerical model was then validated with a particle deposition experiment. A wind tunnel experiment was carried out to quantify the particle deposition on the semi-circular micropatterns for a wide range of heights. Based on our numerical results, the semi-circular pattern height of 500 μm with a pitch-to-height ratio (p/e) of 10 has 8.58 times enhancement of the energy efficiency compared with a high-efficiency particulate air filter (HEPA). Our results indicated that adding surface micropatterns to ventilation ducting for submicron particle deposition is a possible energy-efficient air cleaning technique for practical usage.

1. INTRODUCTION

The transport and deposition of particles in turbulent ducts, indoor environments, and electronic devices have been widely investigated. In some indoor environments, managing particle deposition can improve occupants' welfare and reduce the risks from exposure to poor air quality (Whicker et al. 2002). There are different sources of particulate matter (PM) and different methods to remove them in order to achieve good indoor air quality. Considering effects on health, PM is typically defined by size, with the smaller particles having a greater impact on health. There are different tools to remove different size of PM, but disadvantages exist in them. An efficient air cleaner is a good household appliance to remove particles larger than 1 μm. However, it is difficult for most air cleaners to remove submicron particles, especially in the range of 0.1 to 1 μm (Shaughnessy et al. 1994). High grade, densely packed fiber filters can remove some of these particles, but such filters are expensive to maintain. Another way to improve the indoor air quality is to enhance particle deposition in commercial ventilation ducting systems. Ventilation ducting systems facilitate fresh air in indoor environments by being receptive to ambient air and re-circulating indoor air. Through ventilation ducts, outdoor particles may be carried indoors, and indoor generated particles may return indoors. Therefore, particle deposition in ventilation ducts has an important influence on building occupants' exposure to particles. The occupants of buildings can breathe cleaner air if more particles are deposited on the ventilation ducts. Most of the current ventilation ducting systems use a high-efficiency particulate air filter (HEPA). Although the filtration efficiency of HEPA can reach up to 99% for submicron particles, the ventilation ducting system also suffers a large pressure drop of 500 Pa (Model H13-P20, Klima-Service Incorporated, CZ). Moreover, the pressure drop increases with dust loading which leads to an unsatisfactory operation procedure due to periodical replacement (Hosseini and Tafreshi 2010; Thomas et al. 2001). Further, the heating ventilation and air conditioning (HVAC) fans required to overcome this pressure drop accounts for 30% of an HVAC system's average energy consumption

(McQuiston and Parker 2004). Overall, HEPA filters are not generally used due to their very high operation cost and high pressure drop. It is valuable to explore other ways that can enhance submicron particle deposition along with reducing the pressure drop.

A novel technique needs to be implemented for ventilation ducts to capture submicron particles and reduce their concentration before entering the indoor space. The particle deposition on ventilation ducting walls has been understood extensively both theoretically and experimentally. Lai (2002) reviewed indoor airborne particle loss in room-sized and non-room-sized enclosures based on particle size range, enclosure dimensions, the mixing mechanism and surface texture. The deposition mechanism for reviewed data was based on Brownian motion, turbulent diffusion and gravitational settling. Sippola and Nazaroff (2004) experimentally indicated that surface roughness is the dominant factor for deposition in a ventilation duct. They investigated the influence of particle size, air speed, and deposition surface characteristics. Their results concluded that the deposition velocities to duct ceilings and walls were greatly enhanced in ducts with insulation roughness elements in comparison with steel ducts. Zhao and Wu (2006a) proposed an improved Eulerian model to predict particle deposition velocity by considering turbophoresis as well as Brownian motion, turbulent diffusion and gravitational settling in a fully developed turbulent duct flow. Their model only required friction velocity as the input and then, they applied this model to predict particle deposition velocity onto rough walls (Zhao and Wu, 2006b). They concluded that the dimensionless deposition velocity increases as the dimensionless effective roughness increases, which will cause the flow to separate partly to form a "separated free shear layer" behind the roughness. Lai and Nazaroff (2005) used monodisperse fluorescent tracer particles to study the deposition of 0.9 to 9 μm monodisperse particles onto vertical walls with a sandpaper roughness ranging from 10 to 250 μm. It is confirmed that the deposition rate increases significantly with the increase of roughness, and it becomes a constant when the roughness is large enough. Most researchers parameterized surface roughness based on surface roughness height,

moreover, Hussein et al. (2012) considered two roughness parameters and generalized the models by proposing a dimensionless number: the ratio of surface roughness height to the peak-to-peak distance. Subsequently, Lai et al. (1999; 2001) compared particle deposition rate in smooth and ribbed duct air flow by experimental measurement. Their results indicated that the ribbed wall with the rib pitch-to-height ratio of 10 could significantly enhance the 0.7 to 7.1 μm particle deposition rate. But the deposition mechanism by a patterned surface is still not well understood until flow field numerical simulation works. Lu and Lu (2015a; b; 2016) investigated the effects of surface rib arrangements on particle deposition in two-dimensional ribbed duct air flows by the numerical method. They explained that a larger number of particles were intercepted by the recirculation flow between the surface ribs, where the submicron particles can reach the highest enhancement. It is beneficial to use regular patterned surfaces to deposit more submicron particles in a ventilation duct.

Previous studies show that patterned surfaces can enhance the deposition of submicron particles. Since such patterned surfaces are convenient to change, this is also a simple and economical way to integrate an air cleaning function in ventilation ducts. The pressure drop increase along the ventilation duct will cause the fan energy to overcome this resistance, and, therefore, increasing HVAC system's average energy consumption. In order to compromise the overall performance of energy consumption increase and particle deposition enhancement by various pattern shapes and different value of pitch-to-height ratio (p/e), the shape of semi-circular have been selected to reach the best efficiency in comparison with the shape of triangular, rectangular and open-circular patterned surface (Xu et al. 2019). Lotus leaves are known to be very effective in collecting airborne particles (Beckett et al. 1998). Stemming from the leaves is a hierarchical surface structure which is semi-circular in shape (Bhushan and Her 2010). Another natural trait is inspired by shark skin that can reduce fluid drag effectively in the turbulent flow regime (Bechert et al. 2000). Dean and Bhushan (2010) found that circular riblets cause a reduction in shear stress at the surface,

when comparing drag reduction from a blade riblet, an open triangle and an open circle shape, which all represent different patterns on a shark's surface. These natural traits and previous studies indicate that semi-circular patterns can enhance particle deposition as well as reduce fluid drag in the turbulent flow. Since the smallest scale in turbulent flow can go down to the micrometer level, if the patterned structure on the wall surface is at the micrometer-scale, the two scales become comparable and interaction is manifested. By optimizing the micro patterns' height and *p/e* value, the deposition enhancement could be maximized.

In this research, there are three main objectives: firstly, to investigate the effects of pattern height and *p/e* value on deposition velocity for submicron and micron-sized particles by both numerical and experimental approaches; secondly, to find the area-weighted ratio for the flow field at upstream, center and downstream between two consecutive semi-circular ribs to calculate the experimental deposition velocity; thirdly, to compare the differential pressure weighted deposition enhancement between a patterned surface and a HEPA filter. Particle deposition enhancement on a semi-circular surface in turbulent flows was examined by using computational fluid dynamics simulation. A particle deposition experiment was carried out to validate our numerical results for a wide range of pattern heights and particle sizes. The height of semi-circular patterns in the numerical set-up is 2000 μm, 1500 μm, 800 μm and 500 μm. In order to compare with other benchmark cases in Lu and Lu (2015a; b; 2016), the highest semi-circular rib is set to be 2000 μm. The semi-circular height of 500 μm is the lowest resolution we can fabricate by using 3D priting in our experiment. The *p/e* value varied from 3 to 10 with particle diameters of 0.1, 0.2, 0.3, 0.5, 1, 2, 3 μm. The smallest *p/e* is 3 for our semi-circular ribs (the ratio of semi-circular base to height is 2) and the largest *p/e* is 10 in order to determine the optimized *p/e* ratio under different heights. For the particle size, we focused on submicron particles. However, particles larger than 1 μm are used to observe the whole trend of particle deposition enhancement under various relaxation times. Finally, the benefits of our

designed patterned surface are compared with a HEPA filter in a ventilation duct to indicate the best efficiency index.

2. NUMERICAL METHODOLOGY AND VALIDATION

2.1 Turbulent air flow and Lagrangian particle tracking

The particle deposition on a micropatterned surface was studied numerically. Computational fluid dynamics simulation (CFD) methods have been used to predict the particle deposition by applying different numerical models (Tao et al. 2017). Gao et al. (2012) compared the capability and accuracy of three Reynolds-averaged Navier–Stokes equations (RANS) turbulence model, a Re-normalization Group (RNG) $k-\varepsilon$ model, a Shear Stress Transport (SST) $k-\omega$ model and a Reynolds stress model (RSM) to distinguish the three deposition regimes. They concluded that the RSM model with near-wall corrections obtained a more reasonable prediction of deposition rate of particles less than 1 μm than the SST $k-\omega$ and RNG $k-\varepsilon$ models. Besides, Mehel et al. (2010) took the recommendation of enhanced wall treatment combined with near-wall correlations in the RSM model. Their results yield very satisfactory predictions over the whole range including inertia, diffusion and diffusion-impaction regime. In this research, the Reynolds stress model (RSM) was coupled with a discrete random walk model to reproduce the instantaneous velocity field and a one-way coupled Lagrangian approach was employed to solve each particle trajectory. ANSYS Fluent 16.1 with UDF near-wall correlations was used. The second-order upwind scheme was used for solving the momentum equation and additional transport equations associated with the RANS models. Here, u_i' is the instantaneous flow velocity and the overbar represents an average. The governing equations for mass and momentum conservation are demonstrated by Equation (1) and (2).

$$\frac{\partial \overline{u_i}}{\partial x_i} = 0 \tag{1}$$

$$\frac{\partial \overline{u_i}}{\partial t} + \overline{u_j}\frac{\partial \overline{u_i}}{\partial x_j} = -\frac{1}{\rho}\frac{\partial \bar{p}}{\partial x_i} + \frac{1}{\rho}\frac{\partial}{\partial x_j}\left(\mu\frac{\partial \overline{u_i}}{\partial x_j} - \rho\overline{u_i' u_j'}\right) \tag{2}$$

where $\overline{u_i}$ is the time-averaged velocity, $\bar{p}$ is the time-averaged pressure, μ is the dynamic viscosity of the fluid. The anisotropy of turbulence significantly affects the mean flow, thus the corresponding Reynolds stress tensor, $R_{ij} = \rho\overline{u_i' u_j'}$ was evaluated using the Reynolds stress transport model. For incompressible flow the Reynolds stress transport equation can be described by Equation (3). Different terms from Equation (4) - (7) represents the stress production term, pressure-strain redistribution term, turbulent dissipation term and turbulent diffusion term.

$$\frac{DR_{ij}}{Dt} = P_{ij} + \emptyset_{ij} - \varepsilon_{ij} + \frac{\partial J_{ijk}}{\partial x_k} \tag{3}$$

$$P_{ij} = \rho\left(\overline{u_i' u_k'}\frac{\partial u_j}{\partial x_k} + \overline{u_j' u_k'}\frac{\partial u_i}{\partial x_k}\right) \tag{4}$$

$$\emptyset_{ij} = \overline{-p\left(\frac{\partial u_i}{\partial x_j} + \frac{\partial u_j}{\partial x_i}\right)} \tag{5}$$

$$\varepsilon_{ij} = 2\mu\frac{\partial \overline{u_i}}{\partial x_k}\frac{\partial \overline{u_j}}{\partial x_k} \tag{6}$$

$$J_{ijk} = \overline{pu_i}\delta_{jk} + \overline{pu_j}\delta_{ik} + \rho\overline{u_i u_j u_k} - \mu\frac{\partial}{\partial x_k}\left(\overline{u_i u_j}\right) \tag{7}$$

The instantaneous value of the fluid velocity was determined by the summation of mean fluid phase velocity ($\overline{u}$) and fluctuating velocity (u'). Then the turbulent dispersion of particles can be modeled using a stochastic approach by integrating the instantaneous fluid velocity along the particle trajectory. This process needs to compute the trajectory for enough particles (30000 particles released in the current

simulation). In Equation (8), the turbulence eddy is characterized by a Gaussian distributed random velocity fluctuation, $u^{'}$, $v^{'}$ and $w^{'}$.

$$u^{'} = \varsigma\sqrt{\overline{u'^2}}, v^{'} = \varsigma\sqrt{\overline{v'^2}}, w^{'} = \varsigma\sqrt{\overline{w'^2}} \tag{8}$$

where ς is a normally distributed random number between 0 and 1, the remainder of the right-hand side is the local root mean square (RMS) value of the velocity fluctuations. Previous studies showed that turbulent velocity fluctuation in the wall-normal direction has a crucial influence on particle deposition velocity (Tian and Ahmadi 2007; Zhang and Chen 2009). A near wall correction in Equation (9) was applied to the boundary layer when $y^+ < 4.0$ (Lai and Chen 2006; Matida et al. 2000).

$$v^{+'} = Ay^{+2} \tag{9}$$

where $y^+ = yu^*/v$ and $v^{+'} = \sqrt{\overline{v'^2}}/u^*$. Ounis et al. (1991) suggested A as 0.008 by using the DNS analysis of near wall flows. Therefore, the near-wall ($y^+ < 4.0$) turbulence kinetic energy can be altered to Equation (10).

$$k = \frac{\overline{u'^2} + \overline{v'^2} + \overline{w'^2}}{2} = \frac{3(0.008u^*(y^+)^2)^2}{2} \tag{10}$$

The values calculated by Equation (10) are set to the first two rows of the cells next to the wall boundaries. Although the turbulence kinetic energy in Equation (10) remains isotropic, the prediction of the normal component of Reynolds stress term is improved and the particle deposition velocity is more reasonable (Lai and Chen 2006). A fully developed turbulent channel flow profile for the velocity magnitude, turbulence kinetic energy and turbulence dissipation rate were imposed at the inlet (Xu et al. 2019). Fluent Lagrangian Discrete Phase Model (DPM) can accurately model the Brownian diffusion as it physically models the Brownian motion (Zhao et al. 2011). Al Assaad et al. (2019) used DPM and

validated CFD model to track the dispersion of floor-resuspended particles at the particle size of 1 μm and 10 μm. The DPM implemented in Fluent treated the fluid phase as a continuum by solving the Navier-Stokes equations, while the dispersed phase is solved by tracking a large number of particles through the calculated flow field. A total of 30000 particles were uniformly distributed within 30 wall units at the center of the lower channel wall. The Fluent Lagrangian discrete phase model (DPM) was solved by Equation (11) and (12).

$$\frac{du_p}{dt} = F_{drag}(u - u_p) + \frac{g_x(\rho_p - \rho)}{\rho_p} + F_x \tag{11}$$

$$\frac{dx}{dt} = u_p \tag{12}$$

Equation (11) and (12) describe the particle velocity equation and particle trajectory equation. Here, F_{drag} is the particle drag force, g_x is the gravitational acceleration and F_x is additional forces that include Brownian motion force ($F_{brownian}$), and particle lift force (F_{lift}) listed in Table 1. The particle drag force for micron-sized particles is dependent on different particle Reynolds number, which can be defined in Equation (13). For submicron particles, they tend to follow the flow field more quickly and, therefore, the local velocity of each particle can be considered as having the same local velocity of air.

$$Re_p = \frac{d_p|u - u_p|}{\upsilon} \tag{13}$$

where u is the local velocity of air and u_p is the local velocity of the particle. A detailed description of the numerical model and different particle force can also be found in Xu et al. (2019). Equation (14) and (15) define the particle drag force for submicron and micron-sized particles.

$$F_{drag} = \frac{18\mu}{{d_p}^2 \rho_p C_c} \tag{14}$$

$$C_c = 1 + \frac{2\lambda}{d_p}(1.257 + 0.4e^{-\left(\frac{1.1d_p}{2\lambda}\right)})$$

$$F_{drag} = \frac{18\mu}{\rho_p D_p^2}\frac{C_D Re_p}{24}$$

$$C_D = \frac{24}{Re_p} \text{ for } Re_p < 1 \tag{15}$$

$$C_D = \frac{24}{Re_p}(1 + 0.15Re_P^{0.687}) \text{ for } 1 < Re_p < 400$$

2.2 Computational domain and mesh independence study

The computational domain which resembles the experimental setup with semi-circular ribs is displayed in Figure 1(a). The length of the channel is 400 mm and the width of the channel is 20 mm. The distance between the inlet and start of the semi-circular rib is 200 mm. The ratio of rib height to the rib base width was 0.5, which is consistent for all cases. The "pitch" and "height" are represented in Figure 1(a). The average inlet velocity is 6 *m/s*. At the outlet, the Neumann boundary condition was applied. No slip boundary condition and adiabatic boundary condition were applied to the upper and lower of the pattern wall. An unstructured mesh with fine grid combined with 11 inflation layers (the Y-plus for the first inflation layer is 1.13) around the semi-circular structured surfaces and a coarse grid for the free stream flow was employed, as shown in the bottom subfigure of Figure 1(a). Figure 1(b) displays the grid independence study for the turbulence kinetic energy along the center of the channel for three different meshes (43,293, 70,430 and 113,407 cells). It can be observed that the local turbulence kinetic energy calculated in the cases of 70,430 and 113,407 cells overlap with each other. Therefore, our numerical cases applied the cell density of 70,430.

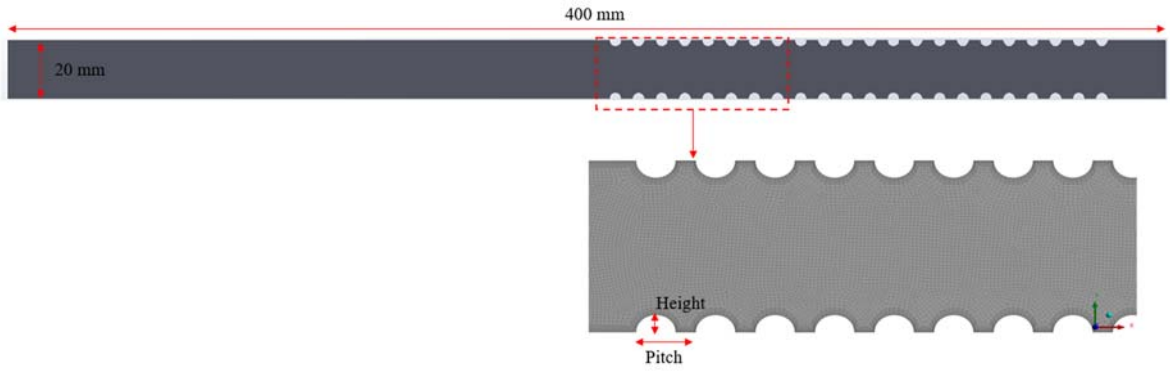

(a)

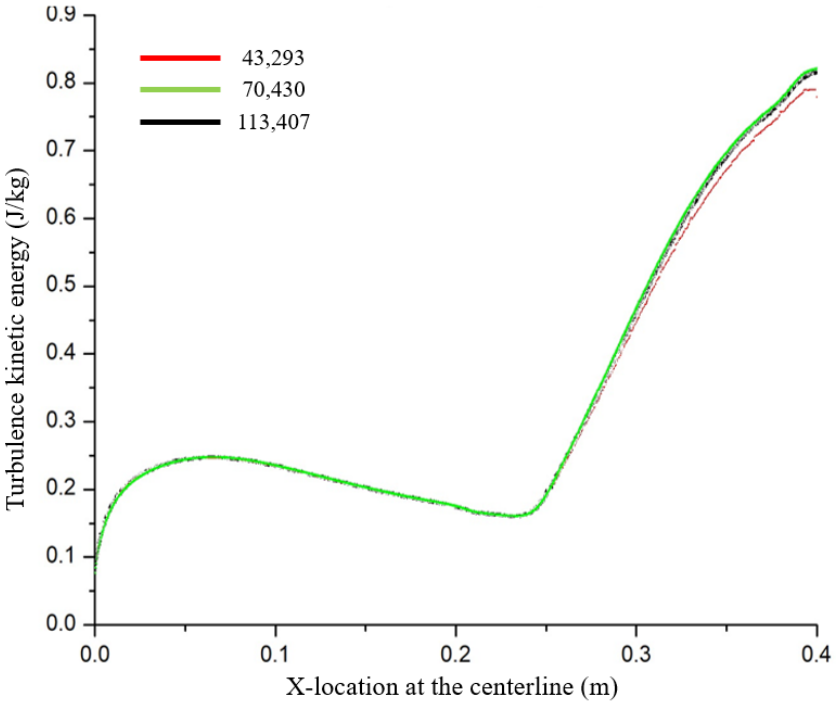

(b)

Figure 1 (a) Computational domain of semi-circular patterned surfaces and mesh distribution (b) Turbulence kinetic energy along the centerline of the channel for three different mesh size

3. VALIDATION WITH EXPERIMENTAL RESULTS

3.1 Experimental setup and methodology

In order to validate the numerical model, a wind tunnel was used to provide a fully developed turbulent airflow. The bottom subfigure in Figure 2(a) illustrates the isometric view of the ribbed surface, where the upper left figure represents pitch and height. The size of the ribbed surface was 75 mm×25 mm. Each ribbed surface was attached to the test section by double-sided tape. As shown in Figure 2(a), the wind tunnel consists of a blower, honeycomb-screens, a long channel of more than 3 m, test section and diffuser (Fu et al. 2014). The honeycomb shaped component plus the screens are effective for removing swirl and lateral mean velocity variations. The honeycomb is used to remove twist from the flow and redirect all flow down the axis of the wind tunnel. To further reduce the amount of turbulence in the flow, Mehta and Bradshaw (1979) recommend a series of turbulence reducing screens. The screens are recommended to go from a low mesh size for the first screen to a high mesh size for the final screen. A longer settling distance allows the flow to stabilize before entering the test section. Unstable flow entering the test section would cause flow separation resulting in additional turbulence. The channel measured 20 mm in height, 200 mm in width with the test section located 3 m downstream along the duct in order to stabilize the flow and was at 150 times the height of the channel. The duct was made entirely from transparent Perspex. Further, a holder was prepared in order to fix the sample on the centerline of the duct, and a blower driven by a frequency inverter at 275 *Hz* induced airflow into the duct at a free stream velocity of 6 *m/s*. This free stream velocity is similar to the air velocity in ventilation supply ducts. Equation (16) displays the relationship between the friction velocity and the pressure drop in a fully developed channel flow (Pope 2001). For a fully developed flow, the friction velocity u^* is related to the pressure drop per length in the downstream direction *dp/dx* in Equation (16).

$$u^* = \sqrt{-\frac{h}{2\rho}\frac{dp}{dx}} \tag{16}$$

where h is the height of the channel, and ρ is the density of air. By comparing the measurement of pressure drop and the friction velocity using a particle image velocimetry system (Fu et al. 2014), it was confirmed that the flow was fully developed at the test section. Based on Equation (16), the friction velocity is calculated as 0.47 *m/s*.

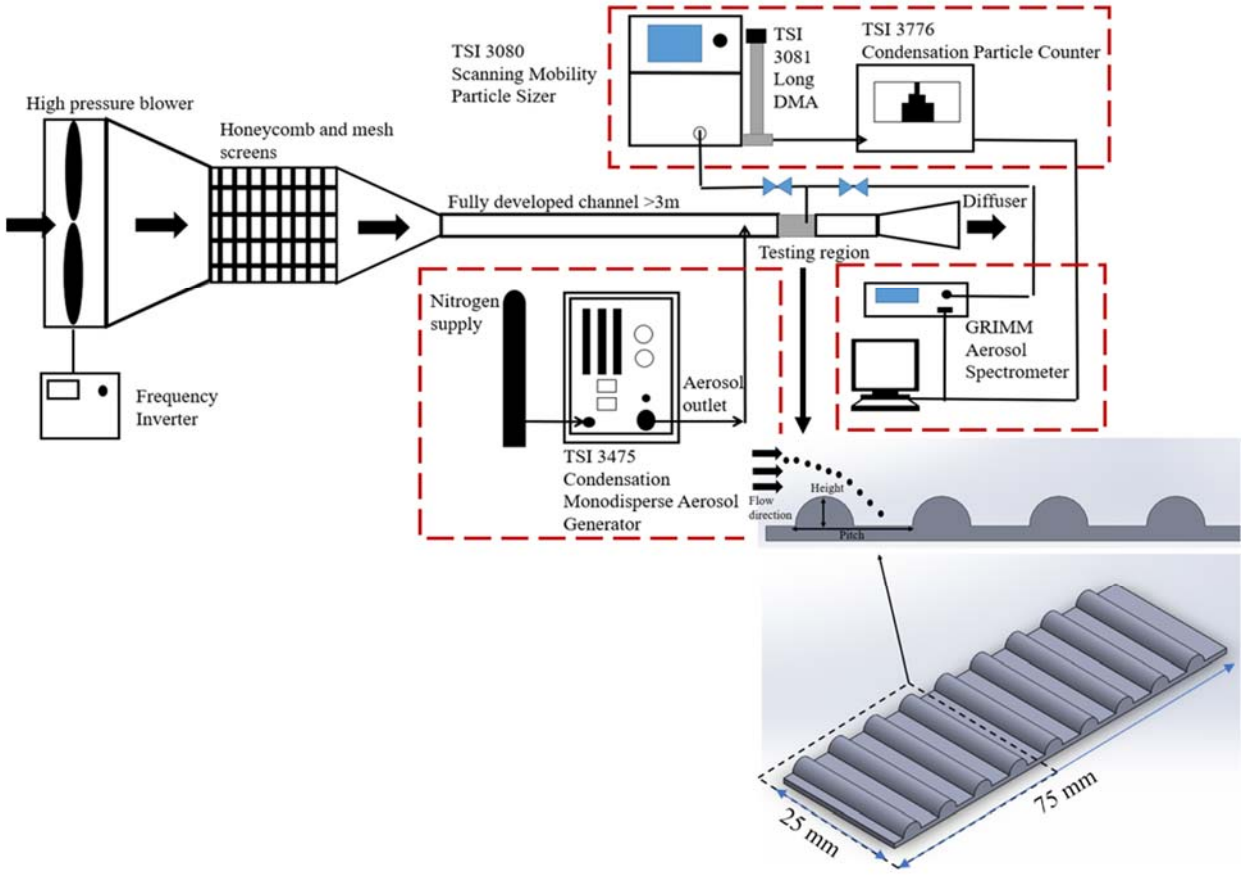

(a)

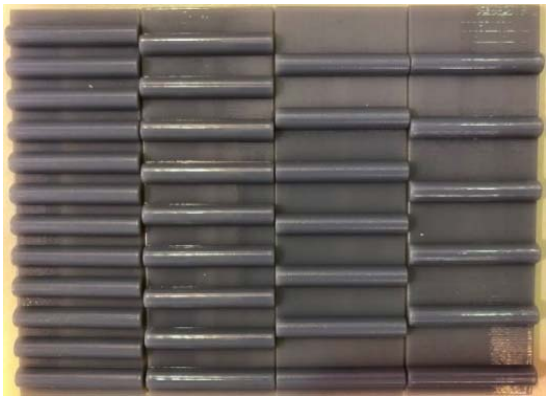

(b)

(c)

Figure 2 (a) Experimental setup and patterned surface for the semi-circular height of (b) 2000 μm (*p/e* from left to right: 3, 4, 5 and 6) and (c) 500 μm (*p/e* from left to right: p/e=3, 4, 5, 6 and 10)

In our experiment, an aerosol generator (TSI 3475, TSI Incorporated, USA) was used to generate high concentration monodispersed aerosols. Vaporized di-2-ethyl hexyl sebacate (DEHS) was condensed onto sodium chloride (NaCl) particles to form airborne particles. The aerosol generator was able to generate particles with sizes ranging from 0.1 to 8 μm (aerodynamic diameter) with a high monodispersity by adjusting the temperature of the saturator. The geometric standard deviation factor for the aerodynamic diameter from 0.5 to 8 μm is less than 1.15. A compressed nitrogen cylinder was connected to the inlet of the aerosol generator to supply a constant flow rate of 250 *l/h*. The outlet of the aerosol generator was connected downstream of the long channel to continuously release aerosol particles at a concentration of 3×10^9 to 5×10^9 particles/m^3 during the experiment. The flow rate of the aerosol generator is 3.67 *lpm*, and the aerosol density is 912 kg/m^3. An aerosol spectrometer (Model 1.108, GRIMM Aerosol, Germany) was used to monitor the particle concentration (particle number per volume) in the free stream for particles of 2.5 μm or above. A Scanning Mobility Particle Sizer (SMPS 3080, TSI Incorporated, USA) was used to measure the particle number concentration for the particle size from 0.01 to 1 μm. The aerosol flow rates for SMPS and GRIMM Particle spectrometer are 3.0 *lpm* and 1.2 *lpm* respectively. The sampling times for the SMPS and GRIMM spectrometer are 3.43 s and 1 s. Two different heights (2000 μm and 500 μm) of

semi-circular ribbed surface were tested in our experiment, as shown in Figure 2 (b) and (c). All the patterned surfaces were 3D-printed using photopolymer material. The particle deposition velocity, V_d, to a surface is defined as Equation (17).

$$V_d^+ = \frac{J}{n_0 \times u^*} = \frac{particle\ number\ deposited/(area \cdot deposition\ duration)}{particle\ number\ /volume \times friction\ velocity} \tag{17}$$

In Equation (17), J is the particle flux to the patterned surface, n_0 is the particle number concentration per volume. The particle flux is defined as the particle deposition number per area divided by the deposition duration. The particle deposition number is calculated by Equation (18). A detailed derivation of Equation (18) is explained in Section S1 of Supplementary Information.

$$N_d = \frac{2{r_s}^3(2 - 3cos\alpha + cos^3\alpha)}{{d_p}^3 sin^3\alpha} \tag{18}$$

where N_d is the particle deposition number, r_s is the measured contact radius, α is the particle contact angle and d_p is the aerodynamic particle diameter.

3.2 Comparison between experimental and numerical results

In our validation cases, the dimension of simulation geometry is similar to our patterned surface at the bottom subfigure in Figure 2(a). The distance between the aerosol releasing position and the location of the first semi-circular rib in the simulation case identical to the distance between the outlet of the aerosol generator and the patterned surface. In the simulation, all particles are assumed spherical and the particle-particle interaction and re-suspension are not considered. One-way coupling is used and, therefore, the airflow is not affected by the particle motion. As the aerosol liquid attaches to the surface, DEHS can stay for a long time without resuspension. The condensation aerosol generator nebulizes DEHS to produce a high concentration of monodisperse aerosols. The high flow velocity in the wind tunnel creates less chance

of particles being able to collide and coalesce with each other in the air. Although the fluid flow generates considerable removal forces, the liquid aerosols can still attach to the solid surface due to the adhesive force arising from the surface tension of the liquid film. According to the study of liquid aerosol sliding velocity after detachment by Fu et al. (2014), the droplet detachment on three different materials (PMMA, Glass and Stainless Steel) are investigated. They demonstrated the friction velocity to detach liquid aerosol should be at least 1 *m/s* on the PMMA surface. Therefore, our friction velocity in the wind tunnel experiment is under the critical point to detach liquid aerosol. In order to predict the deposition velocity precisely, our numerical model was then validated with experimental results for the submicron and micron-sized particles.

The particle deposition velocity for different *p/e* value of a semi-circular shape between experimental (black) and numerical simulation (red) are compared and displayed in Figure 3. In general, the numerical results are close to the experimental results, and the numerical model was validated by both submicron-sized (0.5 μm) and micron-sized (2.5 μm) particles. From Figure 3 (a) to (d), the bar column for experimental and numerical results follow a similar trend. The semi-circular patterns dominate the surface and the effect of surface roughness for particle deposition can be negligible. The discrepancies between numerical and experimental deposition velocity may be due to the limitation of the microscope. At a larger *p/e* value, it can be indicated from numerical simulation that most particles tend to deposit at the upstream and downstream edge of the semi-circular patterns. These regions are barely observed under the microscope. The overall enhancement calculated will be lower than the numerical results, as shown in Figure 3 (d). Illustrations of particle deposition at different regions between the cavity of semi-circular patterned surface can be found in Section S2 of Supplementary Information. The deposition velocities at the upstream, center and downstream regions for the particle size of 0.5 μm and 2.5 μm at different *p/e* are concluded in the Table S2 and Table S3 (please refer to Supplementary Information). It can be observed as the *p/e* value increases, the downstream of the cavity has more particles deposited compared with the upstream of the

cavity. The overall deposition velocity for larger *p/e* value decreases, and therefore, the optimized *p/e* appears in the middle values of *p/e*.

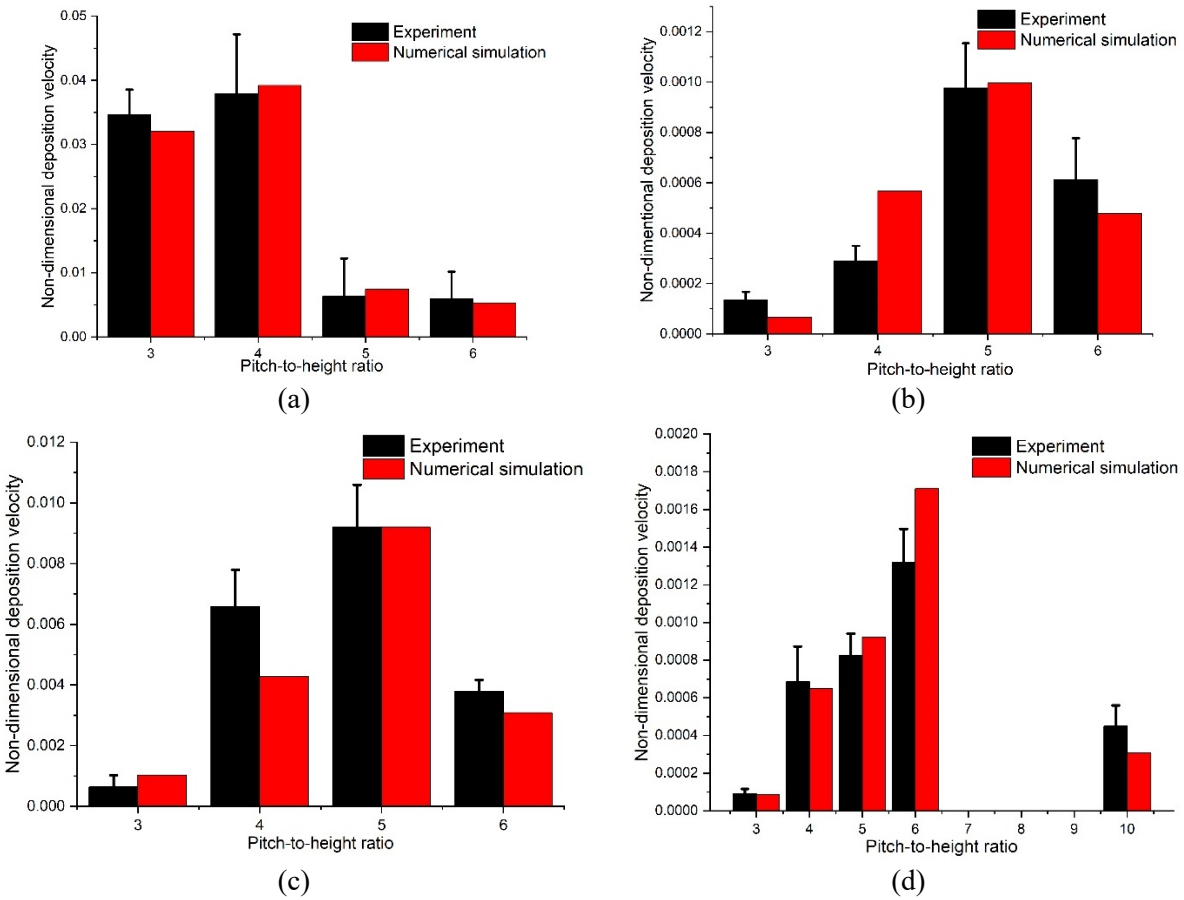

Figure 3 Comparison of non-dimensional deposition velocity between experimental (black) and numerical simulation (red) at the semi-circular height of 2000 μm for the particle size of (a) 2.5 μm and (b) 0.5 μm and semi-circular height of 500 μm for the particle size of (c) 2.5 μm and (d) 0.5 μm

4. NUMERICAL RESULTS AND DISCUSSION

4.1 Particle deposition in the cavity

Our numerical simulation showed that the location for deposition of submicron particles mainly happened at the cavity of two semi-circular ribs (upstream, center and downstream). The flow field to induce particle trajectory in Figure 4 can refer to Section S3 of Supplementary Information. The height of

semi-circular rib in Figure 4 is 500 μm and the *p/e* is 10. The particles follow the recirculation and separation flow to deposit on the bottom surface of the cavity. However, fewer particles deposit at the windward side of semi-circular ribs. In Figure 4(a), particles follow the upward flow into the cavity. In Figure 4(b), some of the particles follow the separation flow to the center of the cavity. As shown in Figure 4(c) and (d), most of the particles tend to accumulate upstream of the cavity, as illustrated by the red rectangular region. The red circle in Figure 4(c) represents where a small vortex formed, and few particles were dispersed into the high-vorticity region. In Figure 4(d), the particle swirl region is clearer because many of the particles enter the red circle. However, some of the particles still follow the mainstream to downstream of the cavity. As more particles flow into the swirl flow region, they disperse close to the solid wall in Figure 4(e) and deposit on the surface. Based on our numerical simulation results, the submicron particles tend to deposit at the bottom surface between cavities. The effect of riblet interception can only deposit fewer particles because the submicron particles have lower mechanisms of inertia impaction compared with the diffusion regime.

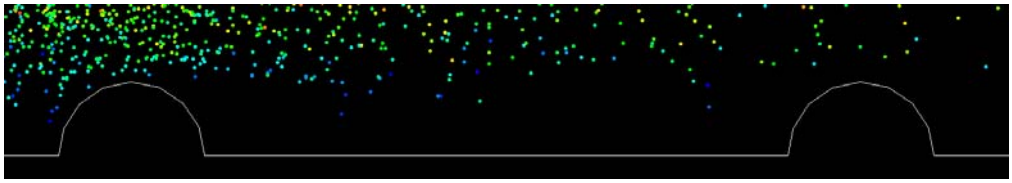

(a)

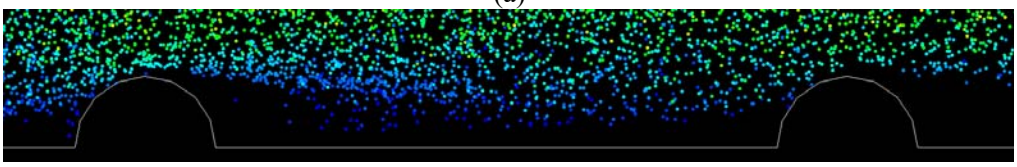

(b)

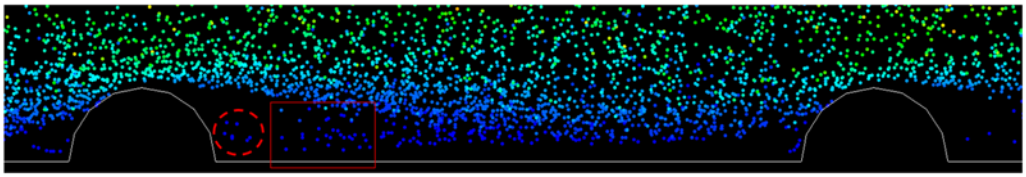

(c)

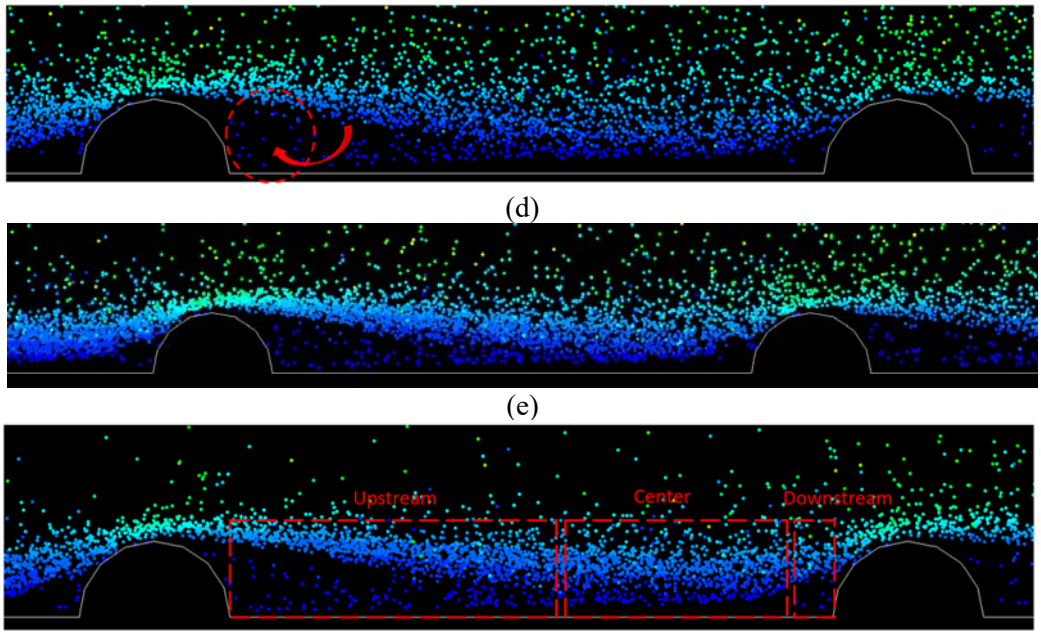

Figure 4 0.5-μm particle trajectory at different time steps (*p/e*=10): (a) 0.005 s (b) 0.007 s (c) 0.009 s (d) 0.011 s (e) 0.013 s (f) 0.015 s

4.2 Particle deposition velocity and deposition enhancement

In this section, we investigated the deposition effect of different heights and different pitch to height ratio of semi-circular patterns. The particle sizes simulated were 0.1, 0.2, 0.3, 0.5, 1, 2 and 3 μm in diameter. The non-dimensional particle deposition velocity and relaxation time can be estimated by Equation (19) and Equation (20). In Equation (19), N_d is the number of deposited particles in the time duration of t_d^+, N_0 is the initial particle number uniformly distributed, y_0^+ is the particle distribution region within a certain distance from the wall, and the superscript '+' means normalization by the wall units, S is the particle to air density ratio, d_p is the particle diameter, υ is the air kinematic viscosity and C_c is the Stokes Cunningham correlation.

$$V_d^+ = \frac{N_d/t_d^+}{N_0/y_0^+} \tag{19}$$

$$\tau^+ = \frac{Sd_p^2 u^{*2}}{18\upsilon^2} C_c \tag{20}$$

The normalization of y_0^+ and t_d^+ are done by the wall unit, as shown in Equation (21) and (22).

$$y_0^+ = \mathrm{y}\frac{u^*}{\upsilon} \tag{21}$$

$$t_d^+ = \mathrm{t}\frac{u^{*2}}{\upsilon} \tag{22}$$

The particle deposition enhancement ratio is defined as the ratio of deposition velocity of a patterned surface to the deposition velocity of a smooth surface, in Equation (23).

$$\phi = \frac{V_{d-rough}}{V_{d-smooth}} \tag{23}$$

where $V_{d-pattern}$ and $V_{d-smooth}$ are the particle deposition velocity of a semi-circular micropatterned surface and smooth surface, respectively. Figure 5 compares the particle deposition enhancement under different *p/e* value for different heights of semi-circular patterns. From Figure 5(a), (b) and (c), the *p/e* value of 4 has the best particle deposition enhancement. The maximum enhancement ratio can reach 5009, 4132, 2773 and 2372 for the semi-circular height of 2000 μm, 1500 μm, 800 μm and 500 μm when the non-dimensional relaxation time is 0.0606 (with a particle size of 1 μm). The enhancement ratio increased from submicron particles to the particle size of 1 μm, and then decreased for the micron-sized particles. As the relaxation time increases, the turbulent diffusion effect will decrease. The enhancement ratio for larger particles also decreases when the non-dimensional relaxation time exceeds 0.06. The larger particles have no time to respond to the changes in the near-wall flow motions by the semi-circular patterned. Instead, their motion is only affected by the larger eddies in the bulk of the flow. For all particle sizes at different *p/e* value and semi-circular heights, the enhancement ratio is always above 1. The maximum enhancement ratio with a semi-circular height of 500 μm changed to a *p/e* value of 10. The lowest enhancement ratio among all the *p/e* values is at 10 for the semi-circular height of 2000 μm and 1500 μm;

while the lowest enhancement ratio is at 3 for the semi-circular height of 800 μm and 500 μm. The enhancement ratio for different *p/e* value can be separated clearly when the pattern height is 500 μm, as shown in Figure 5(d). At a greater height, the enhancement effect for a single rib is too large, dominating the *p/e* effect. Therefore, the influence of *p/e* value moves closer for the higher semi-circular ribs. At a smaller height of semi-circular rib, the various *p/e* effect dominates the particle deposition enhancement. This can explain why the separation of enhancement ratio curves for different *p/e* increases as the height of semi-circular rib decreases from 2000 μm to 500 μm.

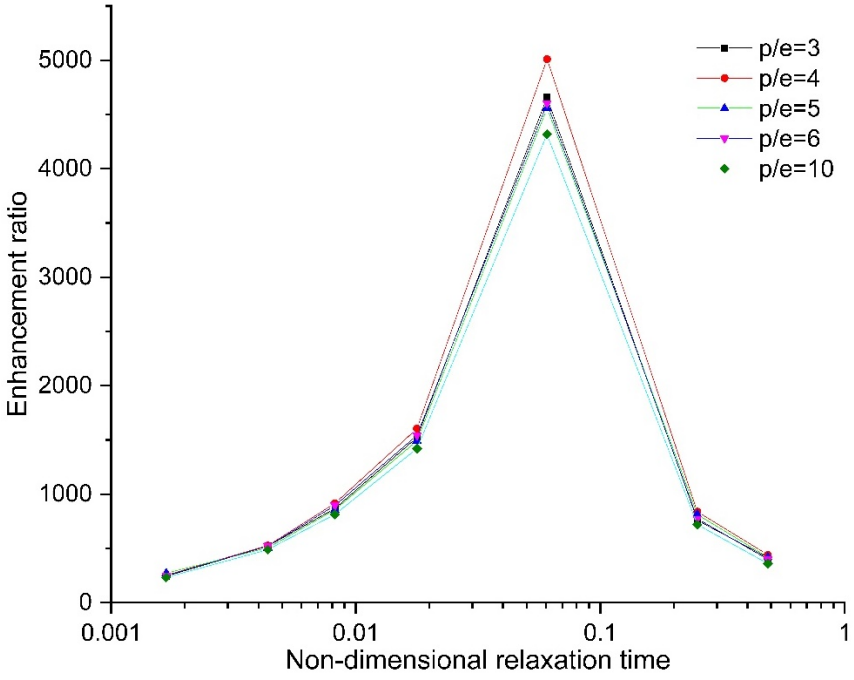

(a)

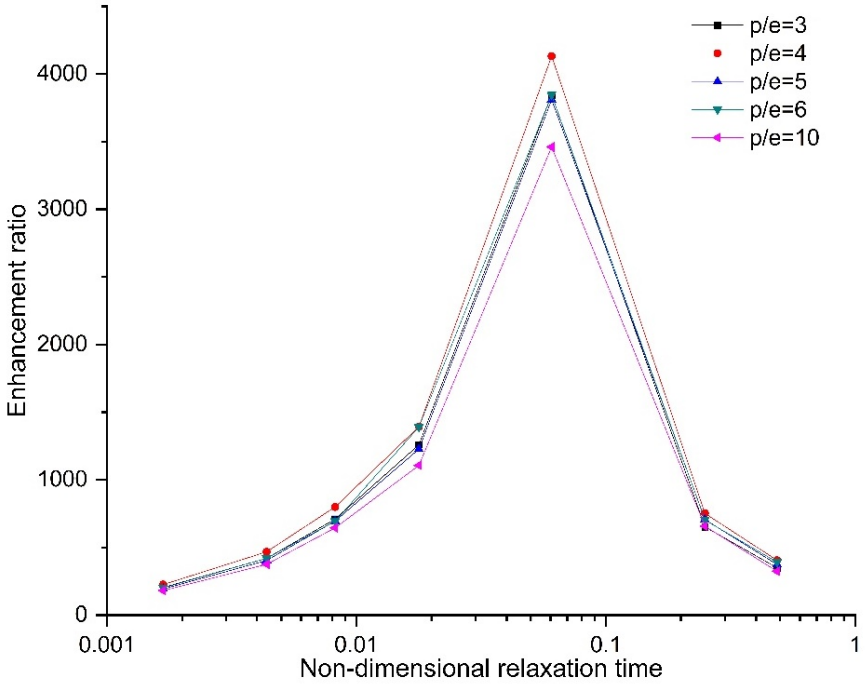
p/e=3
p/e=4
p/e=5
p/e=6
p/e=10
Enhancement ratio
0
1000
2000
3000
4000
0.001
0.01
0.1
1
Non-dimensional relaxation time

(b)

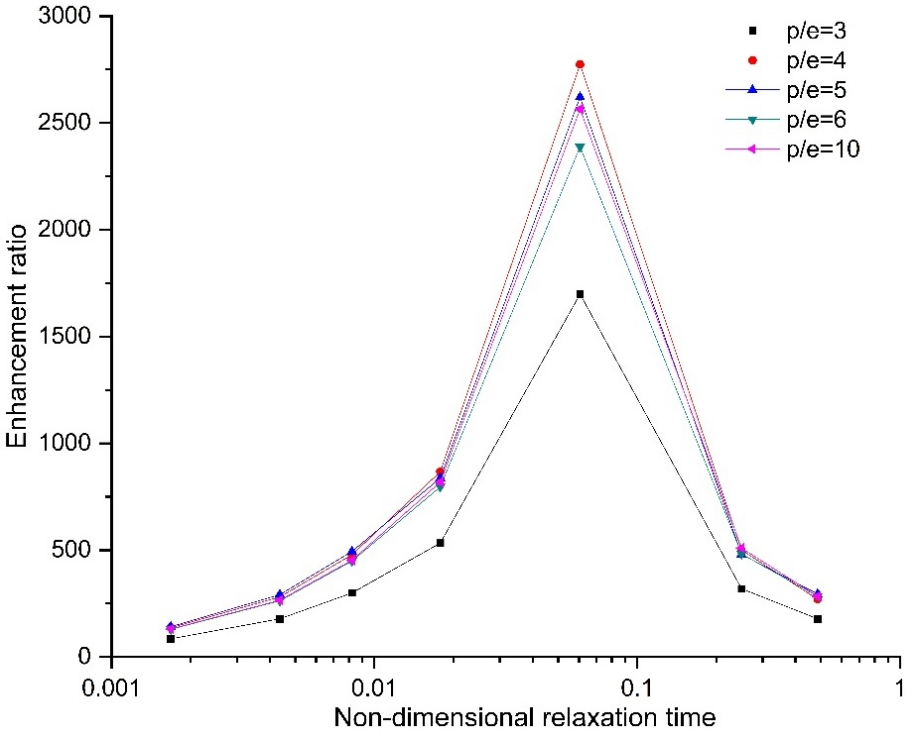
p/e=3
p/e=4
p/e=5
p/e=6
p/e=10
Enhancement ratio
0
500
1000
1500
2000
2500
3000
0.001
0.01
0.1
1
Non-dimensional relaxation time

(c)

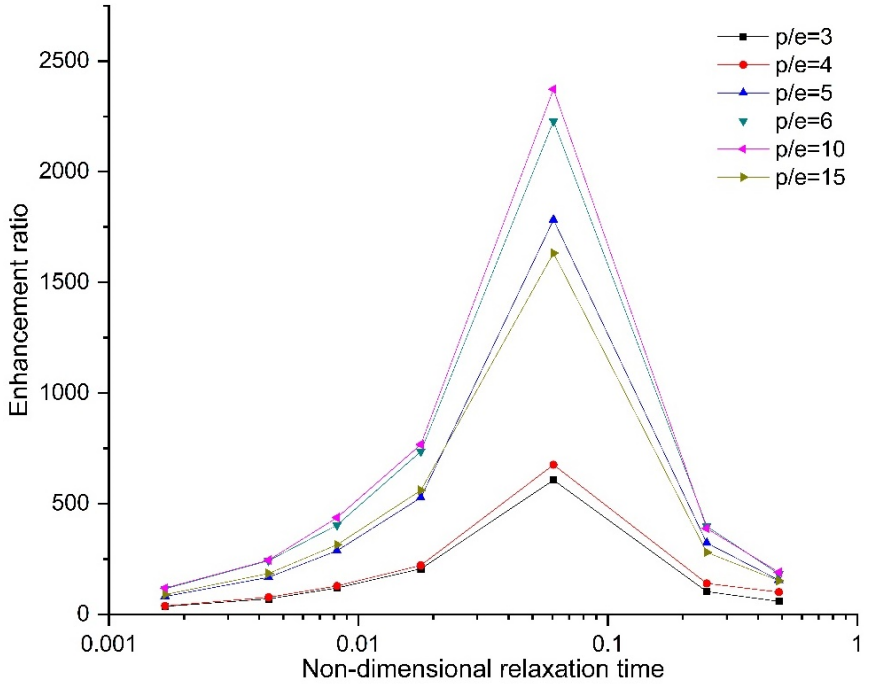

(d)

Figure 5. Comparison of enhancement ratio for different heights of semi-circular patterns: (a) 2000 μm (b) 1500 μm (c) 800 μm (d) 500 μm

4.3 Comparison of efficiency index in ventilation ducting systems

Removal of submicron particles is very difficult due to their small size, but high grade densely packed fibre HEPA (high efficiency particulate air) filters perform well (Wang and Kasper 1991). Joubert et al. (2011) indicated a longer filtration time will impart the particles forming the cake and the water vapor in the air, therefore, resulting in a higher pressure drop during the clogging. It will eventually lead to higher energy consumption in the HVAC fans for air circulation and ventilation. In order to investigate the feasibility of integrating the air cleaning function in ventilation ducts using a patterned surface, an efficiency index η has been defined in Equation (24), which represents a pressure differential weighted particle deposition enhancement (Lu and Lu 2015a).

$$\eta = \frac{V_{d-rough}}{V_{d-smooth}} \cdot \frac{f_{d-smooth}}{f_{d-rough}} \tag{24}$$

where $f_{d-rough}$ and $f_{d-smooth}$ are the friction factors for a semi-circular micropatterned surface and smooth surface, respectively. The pressure drop along the channel for different heights of semi-circular patterns at various *p/e* have been discussed in the Section S3 of Supplementary Information. Figure 6(a) to (d) displays the efficiency index under different heights of a semi-circular patterned surface. Regarding the maximum efficiency index, the semi-circular height of 2000 μm and 1500 μm has a lower value compared with 800 μm and 500 μm. The *p/e* value of 10 at the semi-circular height of 500 μm has the largest efficiency index of 1363 compared with all other *p/e* values among different heights of semi-circular patterns. For the semi-circular height of 2000 μm and 1500 μm, the efficiency index decreases from *p/e* value of 3 to 6. For the semi-circular height of 800 μm, the *p/e* value of 4 has the best efficiency index and a *p/e* value of 3 has the worst performance. The particle deposition enhancement with a *p/e* value of 3 is much lower than any other *p/e* value, and this leads to the lowest efficiency index. Regarding different sizes of particles, the maximum efficiency index always appears at 1 μm. As the particle size increases or decreases, the efficiency index decreases. It shows the efficiency index becomes lower when applied to micron-sized or ultrafine particle deposition. In Lu and Lu (2015a) study, the maximum efficiency of a ribbed surface reached 1000 for smaller particles. The semi-circular micropatterned surface with a height of 500 μm has a much better efficiency index with an improvement compared to the smooth duct of 1363. This improved efficiency is due to the particle deposition enhancement at 2373 times, as well as an increase in the pressure differential of 1.74 times when compared with the smooth duct.

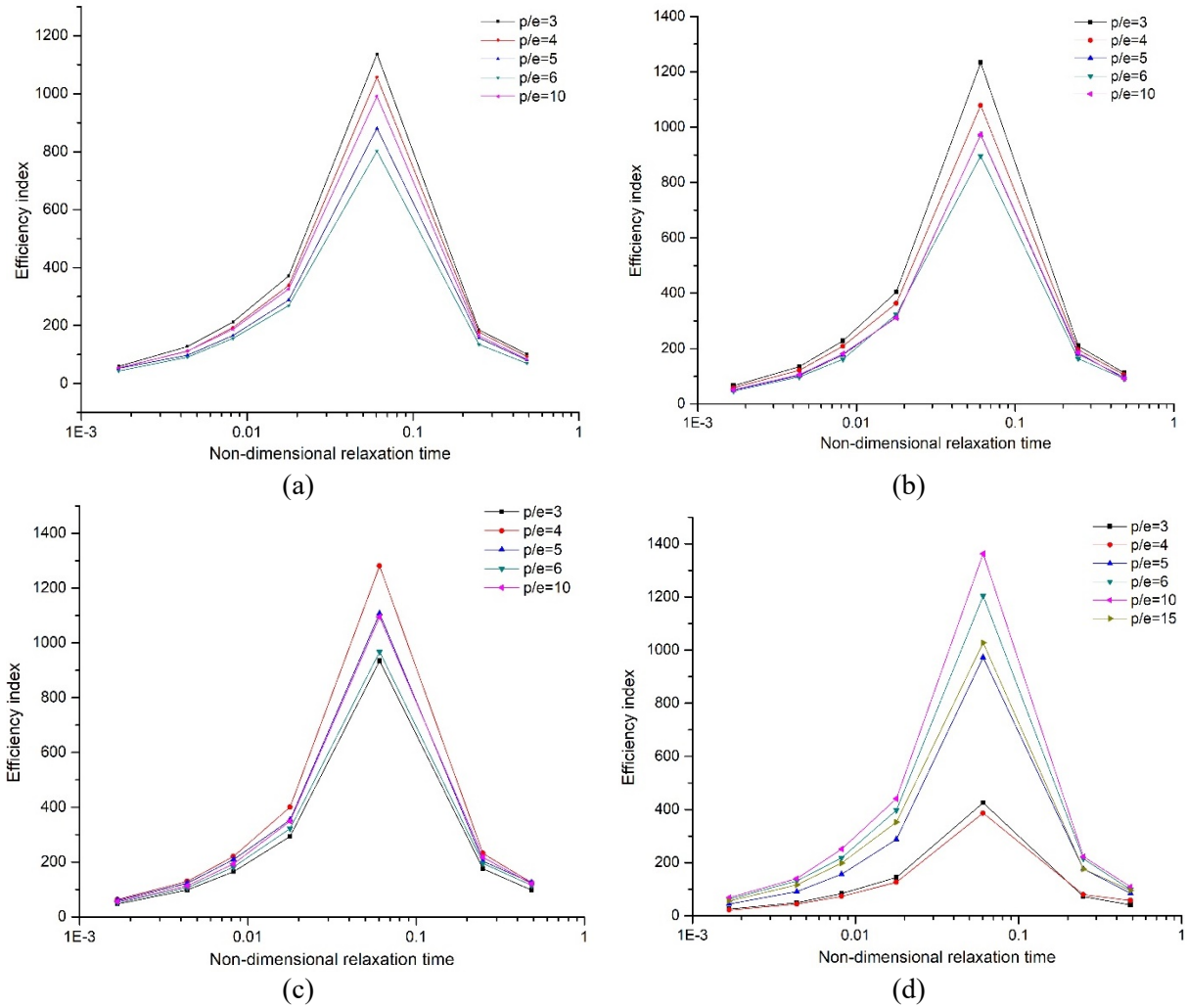

Figure 6. Comparison of efficiency index for different heights of semi-circular patterns: (a) e=2000 μm (b) e=1500 μm (c) e=800 μm (d) e=500 μm

The high-efficiency particulate air filter (HEPA) has been commonly used in current ventilation systems to deposit submicron particles. It can filter the particle size around 0.5 μm with a particle separation efficiency of up to 99.95%, however, it causes a large pressure drop of 500 Pa along the HEPA filter width of 292 mm (Model H13-P20, Klima-Service Incorporated, CZ). In order to compare under similar circumstances, the pressure drop per unit length is used for both HEPA filter and micropatterned surface. If the same number of 0.5-μm particles are released from the duct inlet, the efficiency index can be calculated by Equation (23). Table 1 shows the comparison of efficiency index between the HEPA filter

and micropatterned surface. The best efficiency index of different heights of patterned surface under optimized *p/e* value is listed. Although the non-dimensional deposition velocity of a HEPA filter is much larger than our patterned surface, the efficiency index is smaller than our patterned surface. The significant pressure drop caused by the HEPA filter in the ventilation duct will lead to increased energy consumption in commercial buildings. Moreover, our patterned surface can be reused and cleaned by water if particles have fully loaded the patterned surface, making the cost of our patterned surface lower than the cost of using HEPA filters to reach a similar efficiency index. Therefore, it is recommended that our proposed patterned surface be applied within a ventilation duct to enhance particle deposition as well as to reduce energy consumption.

Table 1. Comparison between HEPA filter and different heights of the patterned surface

	HEPA filter	Patterned surface			
		2000μm (p/e=3)	1500μm (p/e=3)	800μm (p/e=4)	500μm (p/e=10)
Non-dimensional deposition velocity	0.2	0.052	0.043	0.030	0.026
Pressure drop per length (Pa/mm)	1.71	0.0609	0.0464	0.0322	0.0259
Efficiency index	50.79	370.77	402.41	404.56	435.90

5. CONCLUSIONS

This paper reported a fundamental study on particle deposition and proposed a possibility to integrate the air cleaning function in ventilation ducts. Patterned surfaces can enhance particle deposition, but they also cause pressure resistance to the duct. The effect of different *p/e* value of semi-circular patterned surfaces on particle deposition in a turbulent channel flow was presented. A feasibility study of applying semi-circular patterned surfaces as an air cleaning technique in ventilation ducts was conducted

in comparison with the HEPA filter. The overall performance combined with deposition enhancement and increase of pressure drop in the HEPA filter is 50.79. Therefore, we suggest using the semi-circular height of 500 μm at the p/e value of 10, which has the highest efficiency index at 435.90. One limitation is that we only considered liquid aerosol with high adhesive force on the 3D printed patterned surface. In real life, amorphous solid particles with weaker adhesive forces may be more susceptible to detach from the surface. Therefore, further studies could be conducted to investigate different aerosol materials. Another limitation is that our numerical model did not consider the turbophoresis force for small roughness elements on the surface. As the wall roughness is always irregular and complicated, further investigations will be helpful for considering particle turbophoresis to predict the particle deposition velocity from fully turbulent flow onto rough surfaces in ventilation ducts.

FUNDING

The research was supported by Collaborative Research Fund (CRF) project (no. C6022-16G) and HKSAR General Research Fund (GRF) projects (nos. 16207817, and 16206918).

References

Al Assaad, D., Ghali, K. and Ghaddar, N. (2019). Particles dispersion due to human prostration cycle and ventilation system in a prayer room. *Building and Environment* 150:44-59.

Bechert, D., Bruse, M. and Hage, W. (2000). Experiments with three-dimensional riblets as an idealized model of shark skin. *Experiments in fluids* 28:403-412.

Beckett, K. P., Freer-Smith, P. and Taylor, G. (1998). Urban woodlands: their role in reducing the effects of particulate pollution. *Environmental Pollution* 99:347-360.

Bhushan, B. and Her, E. K. (2010). Fabrication of superhydrophobic surfaces with high and low adhesion inspired from rose petal. *Langmuir* 26:8207-8217.

Dean, B. and Bhushan, B. (2010). Shark-skin surfaces for fluid-drag reduction in turbulent flow: a review. *Philosophical Transactions of the Royal Society of London A: Mathematical, Physical and Engineering Sciences* 368:4775-4806.

Fu, S., Leung, W. and Chao, C. Y. (2014). Detachment of droplets in a fully developed turbulent channel flow. *Aerosol Science and Technology* 48:916-923.

Gao, N., Niu, J., He, Q., Zhu, T. and Wu, J. (2012). Using rans turbulence models and lagrangian approach to predict particle deposition in turbulent channel flows. *Building and Environment* 48:206-214.

Hussein, T., J. Smolik, V.-M. Kerminen, M. Kulmala. (2012). Modeling dry deposition of aerosol particles onto rough surfaces. Aerosol Science and Technology 46:44-59.

Hosseini, S. and Tafreshi, H. V. (2010). 3-D simulation of particle filtration in electrospun nanofibrous filters. *Powder Technology* 201:153-160.

Joubert, A., Laborde, J. C., Bouilloux, L., Chazelet, S. and Thomas, D. (2011). Modelling the pressure drop across HEPA filters during cake filtration in the presence of humidity. *Chemical Engineering Journal* 166: 616-623.

Lai, A. C. and Nazaroff, W. (2005). Supermicron particle deposition from turbulent chamber flow onto smooth and rough vertical surfaces. *Atmospheric Environment* 39:4893-4900.

Lai, A. C. (2002). Particle deposition indoors: a review. *Indoor Air* 12:211-214.

Lai, A. C., Byrne, M. A. and Goddard, A. J. (1999). Measured deposition of aerosol particles on a two-dimensional ribbed surface in a turbulent duct flow. *Journal of Aerosol Science* 30:1201-1214.

Lai, A. C., Byrne, M. A. and Goddard, A. J. (2001). Aerosol deposition in turbulent channel flow on a regular array of three-dimensional roughness elements. *Journal of Aerosol Science* 32:121-137.

Lai, A. C. and Chen, F. (2006). Modeling particle deposition and distribution in a chamber with a two-equation Reynolds-averaged Navier–Stokes model. *Journal of Aerosol Science* 37:1770-1780.

Lu, H. and Lu, L. (2015a). Effects of rib spacing and height on particle deposition in ribbed duct air flows. *Building and Environment* 92:317-327.

Lu, H. and Lu, L. (2015b). Numerical investigation on particle deposition enhancement in duct air flow by ribbed wall. *Building and Environment* 85:61-72.

Lu, H. and Lu, L. (2016). CFD investigation on particle deposition in aligned and staggered ribbed duct air flows. *Applied Thermal Engineering* 93:697-706.

McQuiston, F. C. and Parker, J. D. (2004). *Heating, ventilating, and air conditioning: analysis and design*. 6th ed. Wiley

Mehta, R. D. and Bradshaw, P. (1979). Design rules for small low speed wind tunnels. *The Aeronautical Journal* 83:443-453.

Mehel, A., Tanière, A., Oesterlé, B. and Fontaine, J.-R. (2010). The influence of an anisotropic langevin dispersion model on the prediction of micro-and nanoparticle deposition in wall-bounded turbulent flows. *Journal of Aerosol Science* 41:729-744.

Matida, E. A., Nishino, K. and Torii, K. (2000). Statistical simulation of particle deposition on the wall from turbulent dispersed pipe flow. *International Journal of Heat and Fluid Flow* 21:389-402.

Ounis, H., Ahmadi, G. and McLaughlin, J. B. (1991). Brownian diffusion of submicrometer particles in the viscous sublayer. *Journal of Colloid and Interface Science* 143:266-277.

Pope, S. B. (2001). *Turbulent flows*. 1st ed. Cambridge University Press.

Shaughnessy, R. J., Levetin, E., Blocker, J. and Sublette, K. L. (1994). Effectiveness of portable indoor air cleaners: sensory testing results. *Indoor Air* 4:179-188.

Sippola, M. R. and Nazaroff, W. W. (2004). Experiments measuring particle deposition from fully developed turbulent flow in ventilation ducts. *Aerosol Science and Technology* 38:914-925.

Thomas, D., Penicot, P., Contal, P., Leclerc, D. and Vendel, J. (2001). Clogging of fibrous filters by solid aerosol particles experimental and modelling study. *Chemical Engineering Science* 56:3549-3561.

Tian, L. and Ahmadi, G. (2007). Particle deposition in turbulent duct flows—comparisons of different model predictions. *Journal of Aerosol Science* 38:377-397.

Tao, Y., Inthavong, K. and Tu, J. (2017). A numerical investigation of wind environment around a walking human body. *Journal of Wind Engineering and Industrial Aerodynamics*, 168:9-19.

Whicker, J. J., Wasiolek, P. T. and Tavani, R. A. (2002). Influence of room geometry and ventilation rate on airflow and aerosol dispersion: implications for worker protection. *Health Physics* 82:52-63.

Wang, H.-C. and Kasper, G. (1991). Filtration efficiency of nanometer-size aerosol particles. *Journal of Aerosol Science* 22:31-41.

Xu, H., Fu, S. C., Leung, W. T., Lai, T. W. and Chao, C. Y. H. (2019). Enhancement of submicron particle deposition on a semi-circular surface in turbulent flow. *Indoor and Built Environment* 0:1420326X19853862.

Zhao, B. and Wu, J. (2006a). Modeling particle deposition from fully developed turbulent flow in ventilation duct. *Atmospheric Environment* 40:457-466.

Zhao, B. and Wu, J. (2006b). Modeling particle deposition onto rough walls in ventilation duct. *Atmospheric Environment* 40:6918-6927.

Zhao, B., Chen, C. and Lai, A. C. (2011). Lagrangian stochastic particle tracking: further discussion. *Aerosol Science and Technology*, 45:901-902.

Zhang, Z. and Chen, Q. (2009). Prediction of particle deposition onto indoor surfaces by cfd with a modified lagrangian method. *Atmospheric Environment* 43:319-328.

Investigation of particle deposition on a micropatterned surface as an energy-efficient air cleaning technique in ventilation ducting systems

Haolun Xu [a], Sau Chung Fu [b], Ka Chung Chan [b] and Christopher Y.H. Chao [b]

[a] Department of Mechanical and Aerospace Engineering, The Hong Kong University of Science and Technology, Clear Water Bay, Hong Kong

[b] Department of Mechanical Engineering, The University of Hong Kong, Pok Fu Lam, Hong Kong

S1. EXPERIMENTAL METHOGOLOGY TO CALCULATE PARTICLE DEPOSITION VELOCITY

Figure S1 showed the contact angle of DEHS liquid particle on patterned surface. The contact angle measured from Figure S1 is nearly 23° - 25°. The aerosol droplet forms a cap that can be viewed as part of a larger sphere with a radius of R_S. This cap can be viewed as a cut-off from the larger sphere by a plane. The radius of larger sphere in Figure S1 is *AO* and *CO*, which is perpendicular to the red arrow (liquid-vapor interface) at the three-line contact angle. The contact radius in Figure S1 is r_s. The total volume of this spherical cap is similar to the volume of original aerosols deposited and coalesced on the surface. Based on the geometry, the total volume of this spherical cap can be found as Equation (S1).

$$V_{cap} = \frac{1}{3}\pi R_s^3(2 - 3cos\alpha + cos^3\alpha) \quad \text{(S1)}$$

where V_{cap} is the volume of spherical cap, R_s is the contact radius of aerosol and α is the aerosol contact angle. The contact area of the circle can be expressed by Equation (S2).

$$A_{s-l} = \pi r_s^2 = \pi(R_s sin\alpha)^2 \quad \text{(S2)}$$

Combining Equation (S2) with Equation (S1), the contact area of the planar surface can be found as Equation (S3).

$$A_{s-l} = \pi V_{cap}^{2/3}\left[\frac{\pi}{3}(2 - 3cos\alpha + cos^3\alpha)\right]^{-2/3} sin^2\alpha \quad \text{(S3)}$$

The contact area of planar surface can be measured from the microscope. Based on Equation (S3), the volume of aerosol deposited in each picture can be determined.

$$V_{cap} = \left(\frac{A_{s-l}}{\pi\left[\frac{\pi}{3}(2-3cos\alpha+cos^3\alpha)\right]^{-\frac{2}{3}}sin^2\alpha}\right)^{\frac{3}{2}} \quad \text{(S4)}$$

The particle deposition number is calculated by using the total volume of each aerosol droplet divided by the volume of monodispersed spherical aerosol in Equation (S5).

$$N_d = \frac{V_{cap}}{\frac{4}{3}\pi(\frac{d_p}{2})^3} \quad \text{(S5)}$$

Substituting Equation (S4) into Equation (S5), we can obtain the particle deposition number as a function of contact radius, contact angle as well as released particle size.

$$N_d = \frac{2{r_s}^3(2-3cos\alpha+cos^3\alpha)}{{d_p}^3 sin^3\alpha} \quad \text{(S6)}$$

Equation (S6) can be applied to calculate monodispersed particle number in a coalesced larger particle on the surface. For solid particles, attention must be paid to reduce the formation of agglomerates because multi-layers are hard to count (Hinds 2012). However, coagulation or coalescence may occur for liquid particles. There are two kinds of mechanism for liquid aerosol coagulation, either by Brownian motion or by turbulent eddies. For simple monodisperse coagulation, the particle size increases with time according to Equation (S7).

$$\mathrm{d(t)} = d_0(1+N_0Kt)^{1/3} \quad \text{(S7)}$$

where d_0 is the initial particle size, $d(t)$ is the particle size after deposition duration t, N_0 is the particle number concentration for undisturbed flow, and K is the corrected coagulation coefficient which can be checked from (Hinds 2012). The particle size after a long time of

duration for the 0.5 μm particle is still 0.523 μm, which did not change with the particle size. Therefore, the larger particles are due to the coalescence of liquid aerosols on the surface. The resolution of the microscope can barely visualize the particle size smaller than 1 μm, thus a longer particle deposition time allows smaller particles to coalesce together. In order to increase the accuracy of submicron particle deposition, the deposition time in our experiment is almost 2 hours. Therefore, in our experimental methodology, the coalesced aerosol is recognized as a spherical cap that combines numbers of simple monodispersed particles.

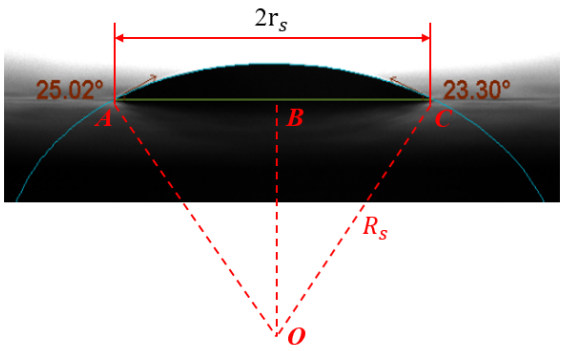

Figure S1 Schematic of DEHS aerosol droplet placed on a flat surface with uniform meniscus radius

Figure S2 displayed a 790 μm×790 μm image from a Nikon eclipse Ni-E Microscope under an object of 20x. The visualized area in each photo is 6.24×10^{-7} m^2. Each blue circle represents a coalesced particle for 0.5-μm monodispersed particle. Take Figure S2 for example, the calculation procedure for the deposition velocity in this figure is shown in Table S1. The contact particle diameter was identified by the Nikon microscope software. Then the volume of each aerosol was determined by using Equation S4. Our experiment has been running for a duration of 5400s, therefore, the released particles will coalesce on the surface. Each identified aerosol consists of several numbers of 0.5-μm particles, and the particle concentration above the patterned surface is 4.67×10^{9} #/m^3. A summation of differently located aerosol will be

the total deposition number. The deposition velocity is calculated by Equation (S8). It should be noted that the deposition velocity in Table S1 is only calculated based on one figure. However, different figures are calculated according to a similar procedure in Table S1 and these values are averaged or area-weighted to gain an overall deposition velocity.

$$V_d^+ = \frac{J}{n_0 \times u^*} = \frac{particle\ \ number\ \ deposited/(area \cdot deposition\ \ duration)}{particle\ \ number\ \ /volume \times friction\ \ velocity} \quad \text{(S8)}$$

Table S1 Calculation of deposition velocity in Figure S2

Contact diameter (μm)	Contact area (μm^2)	Volume (μm^3)	Particle number in each droplet (#)	Total deposition number (#)	Deposition velocity (m/s)
4.14	53.82	23.62	361	929	5.9×10^{-5}
4.12	53.38	23.33	356		
1.98	12.31	2.59	40		
3.23	32.82	11.25	172		

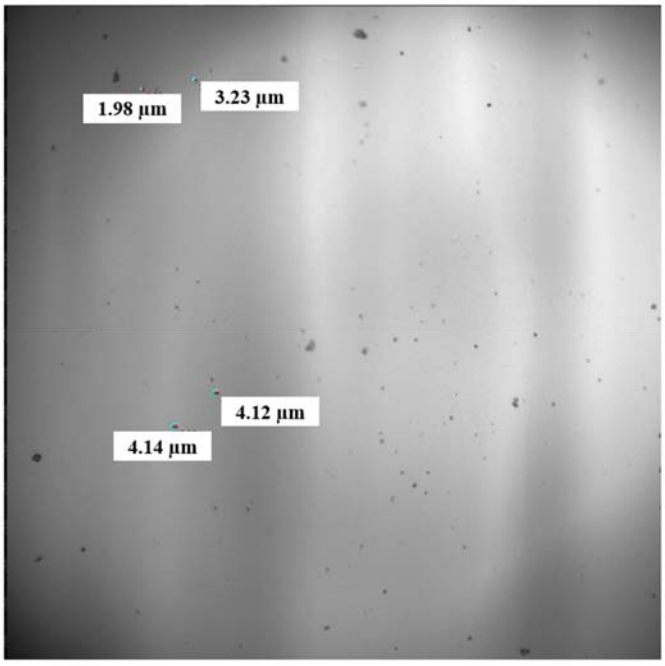

Figure S2 Calculation of deposition velocity

Figure S3 illustrated the surface roughness profile for the 3d printed smooth surface in our experiment. The surface roughness was measured by a Veeco 3300 profiler. The top minor photo in Figure S3 represented a measurement area of 0.627 mm × 0.471 mm. The height between the green arrow and red arrow in the upper minor photo in Figure S3 was 7.513 μm. The bottom photo in Figure S3 showed the surface roughness profile through the horizontal line. It can be seen that the surface roughness oscillates like a sine wave. The averaged surface roughness on our experimental smooth surface was 2.2 μm, but the surface was assumed ideally perfect in our numerical simulation cases. Our current mesh size cannot resolve the surface roughness directly. This may lead to a difference between experimental and numerical results because the surface roughness will also enhance particle deposition.

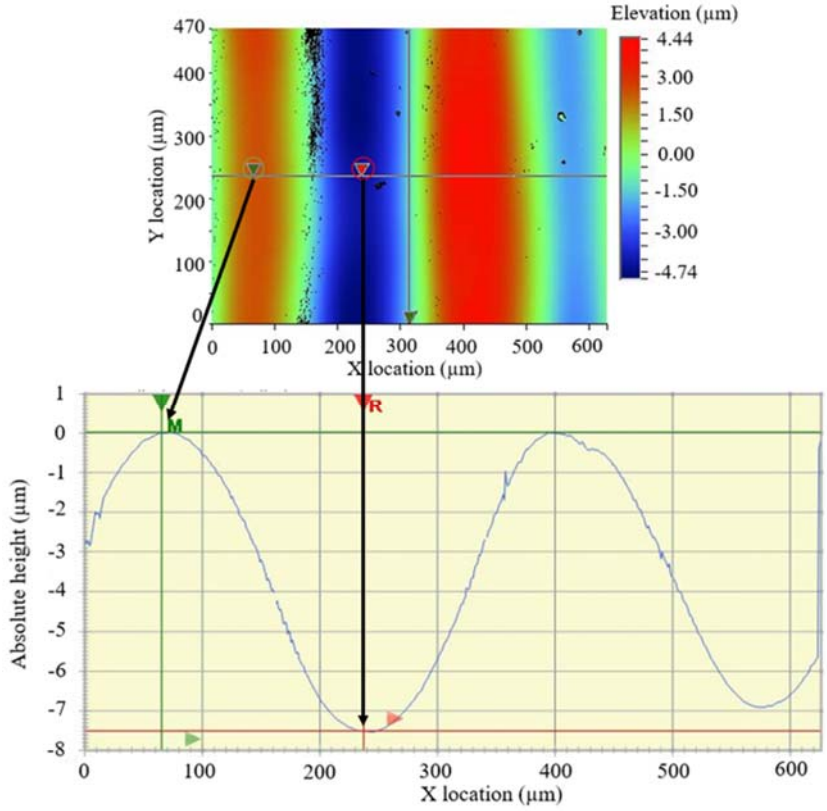

Figure S3 Illustration of surface roughness contour (top) and surface roughness profile (bottom) for a smooth surface

S2. PARTICLE DEPOSITION LOCATION IN THE CAVITY BETWEEN SEMI-CIRCULAR RIBS

The particle deposition location is influenced by the flow patterns within the cavity, and because the flow field for different heights of semi-circular patterned surface is similar, the particle deposition location follows a similar trend for different heights of semi-circular patterned surface. We first discuss the 0.5-μm particle deposition location and deposition velocity on the semi-circular height of 500 μm at the *p/e* value of 3, 4, 5 and 6. Subsequently, the 2.5-μm particle deposition velocity on the semi-circular height of 2000 μm at the *p/e* value of 3, 4, 5 and 6 are demonstrated. The 0.5-μm particle deposition photos for each *p/e* at the height of 2000 μm are shown in Figure S4. Figure S4(a) and (b) shows the particle deposition at the semi-circular ribs where *p/e*=3 and *p/e*=4. Figure S4(c) and (d) shows the particle deposition at the upstream and downstream locations for a *p/e* value of 5. Figure S4(e) and (f) shows particle deposition at the upstream and downstream locations where *p/e*=6. The green circle in the figure represents a clearly visualized particle (the white arrow in Figure S4(a) and (b) identify the particles), and the other black spots are defects on the surface. At the semi-circular patterns where *p/e*=3 and *p/e*=4 as shown in Figures S4(a) and (b), the non-dimensional deposition velocity is 9.3×10^{-5} and 6.86×10^{-4}, respectively. At the *p/e*=5 and *p/e*=6, the downstream location has more particles deposited compared with the upstream location. The larger particles in Figure S4(d) is formed by the coalescence of liquid aerosols on the solid surface. In order to increase the accuracy of submicron particle deposition, the deposition time in our experiment is three hours to allow smaller particles coalesced on the surface. As discussed in the experimental methodology, the coalesced aerosol is recognized as a spherical

cap that combines numbers of simple monodispersed particles. In Figure S4(c) and (d), the non-dimensional deposition velocity at the upstream and downstream is 6.77×10^{-4} and 1.17×10^{-3}. In Figure S4(e) and (f), the non-dimensional deposition velocity at the upstream and downstream is 9.0×10^{-4} and 1.95×10^{-3}. In the case of *p/e*=5, 6 and 10, the deposition velocity can be evaluated from the deposition velocity on different surface areas and can be expressed as Equation (S9).

$$V_{\mathrm{d}} = V_{\mathrm{d,u}} \times l_u\% + V_{\mathrm{d,c}} \times l_c\% + V_{\mathrm{d,d}} \times l_d\% \quad \text{(S9)}$$

where $V_{d,u}$, $V_{d,c}$ and $V_{d,d}$ are deposition velocity at upstream, center and downstream for a patterned surface. l_u, l_c and l_d are area-weighted ratio at upstream, center and downstream region discussed in Table S4. The deposition of 0.5-μm particles for the semi-circular height of 500 μm where *p/e* value is 10 are shown in Figure S5. The non-dimensional deposition velocities in Figure S5 (a), (b) and (c) are 3.43×10^{-4}, 4.74×10^{-4} and 8.88×10^{-4}.

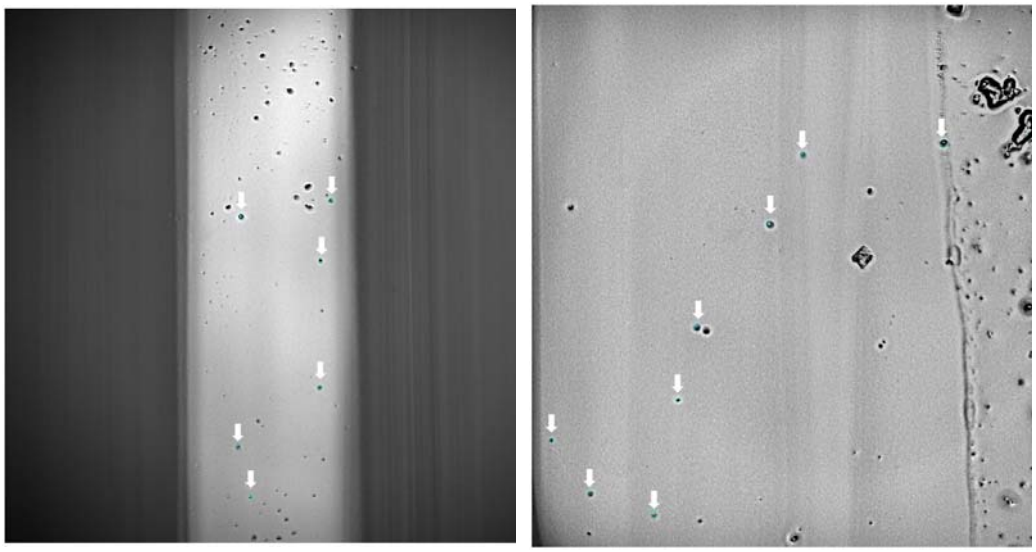

(a) (b)

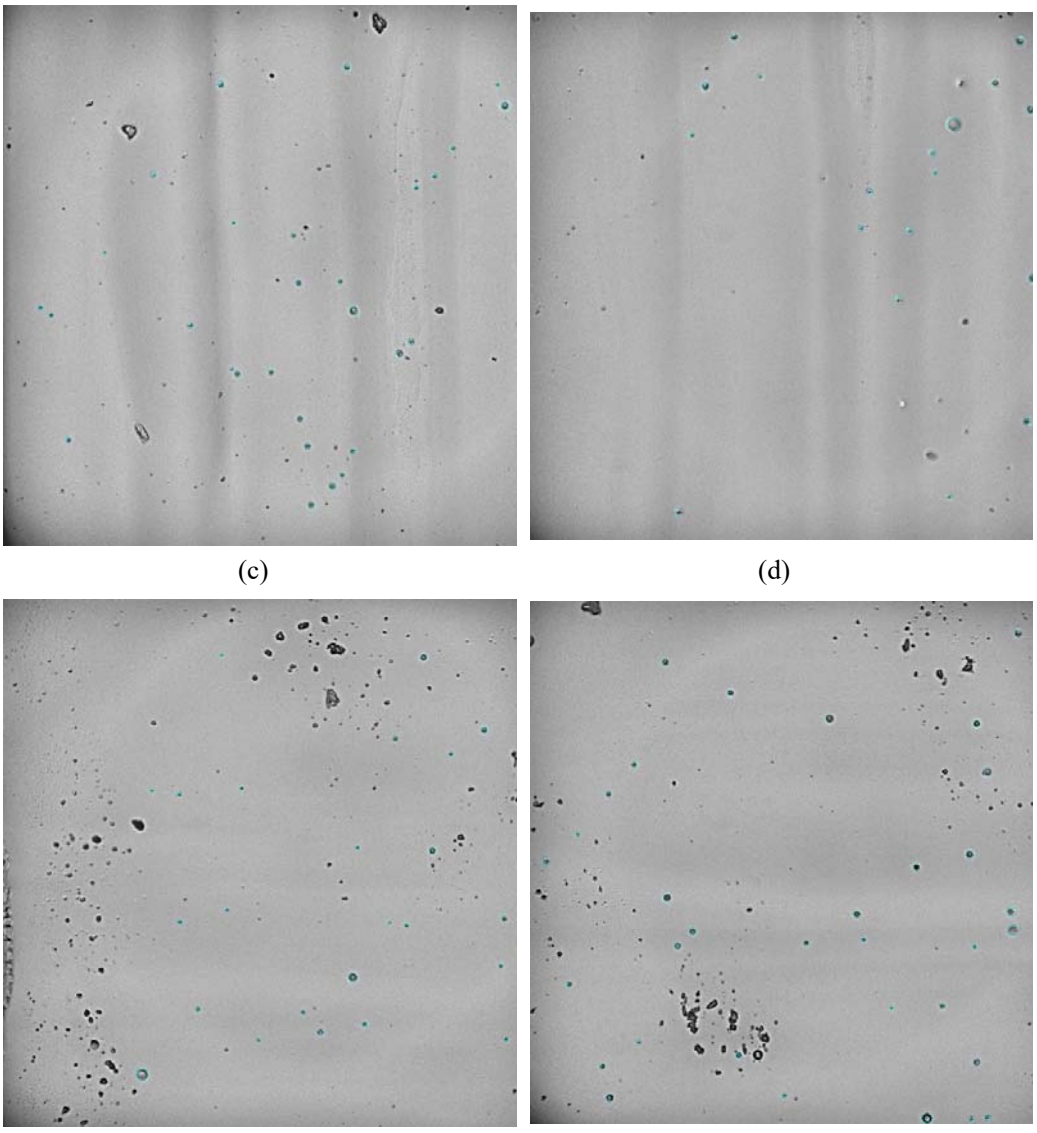

(c) (d)

(e) (f)

Figure S4 Photos after 0.5 μm particle deposition for the semi-circular height of 500 μm: (a) p/e=3 (b) p/e=4 (c) p/e=5, upstream (d) p/e=5, downstream (e) p/e=6, upstream (f) p/e=6, downstream

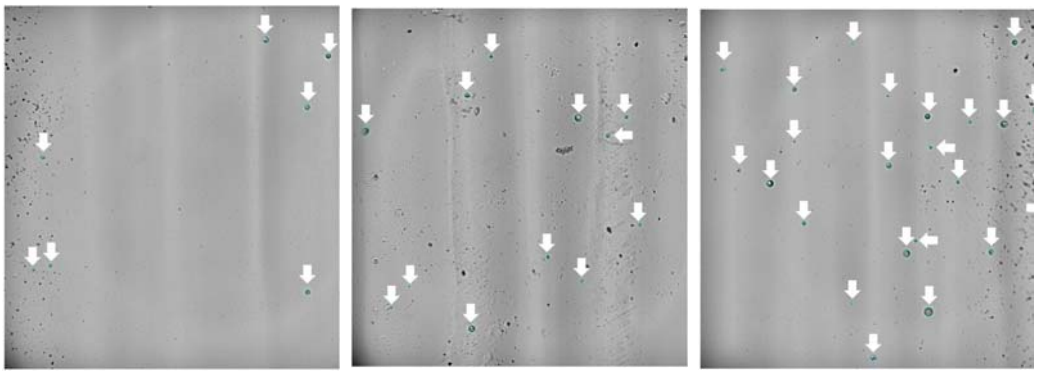

Figure S5 Photos after 0.5 μm particle deposition for the semi-circular height of 500 μm: (a) p/e=10, upstream (b) p/e=10, center (c) p/e=10, downstream

Figure S6 displays 2.5-μm particle deposition for the semi-circular height of 2000 μm at different *p/e* value. Figure S6(a) and (b) shows the particle deposition at the *p/e*=3 and *p/e*=4. Figure S6(c) and (d) shows the particle deposition at the upstream and downstream of the cavity at the *p/e*=5. Figure S6(e) and (f) show the particle deposition at the upstream and downstream of the cavity at the *p/e*=6. Observed from Figure S6(b), the *p/e*=4 has more aerosol particles deposited on the surface compared with other figures. At the *p/e*=5 (Figure S6(c) and (d)) and *p/e*=6 (Figure S6(e) and (f)), the deposition at the downstream location of the cavity has more particles deposited compared with the upstream and center of the cavity. The trend of the deposition enhancement at the upstream and downstream is similar to the discussion in Lai et al. (2000). In their experiment on enhanced particle deposition by a ribbed surface in a ventilation duct, the presence of a downstream rib formed a vortex, thus the highest deposition enhancement appears at the downstream. From our illustration of the streamline (Figure S7(a) and (b)), a small upward swirl flow appears at the downstream location and the direction of flow is opposite to the direction of separation flow at the center region. As the two streams of the flow collide with each other, larger particles deposit due to the effect of inertia impaction, and it is even harder for the particles to change their direction rapidly as the flow moves upward outside the cavity. The deposition at the downstream cavity has a more significant effect than the deposition at the upstream cavity at the *p/e* value of 5 and 6. Based on the above analysis of deposition velocity at different locations, the ratio of deposition velocity at different locations can be concluded in Table S2 and Table S3 for the particle size of 0.5 μm and 2.5 μm.

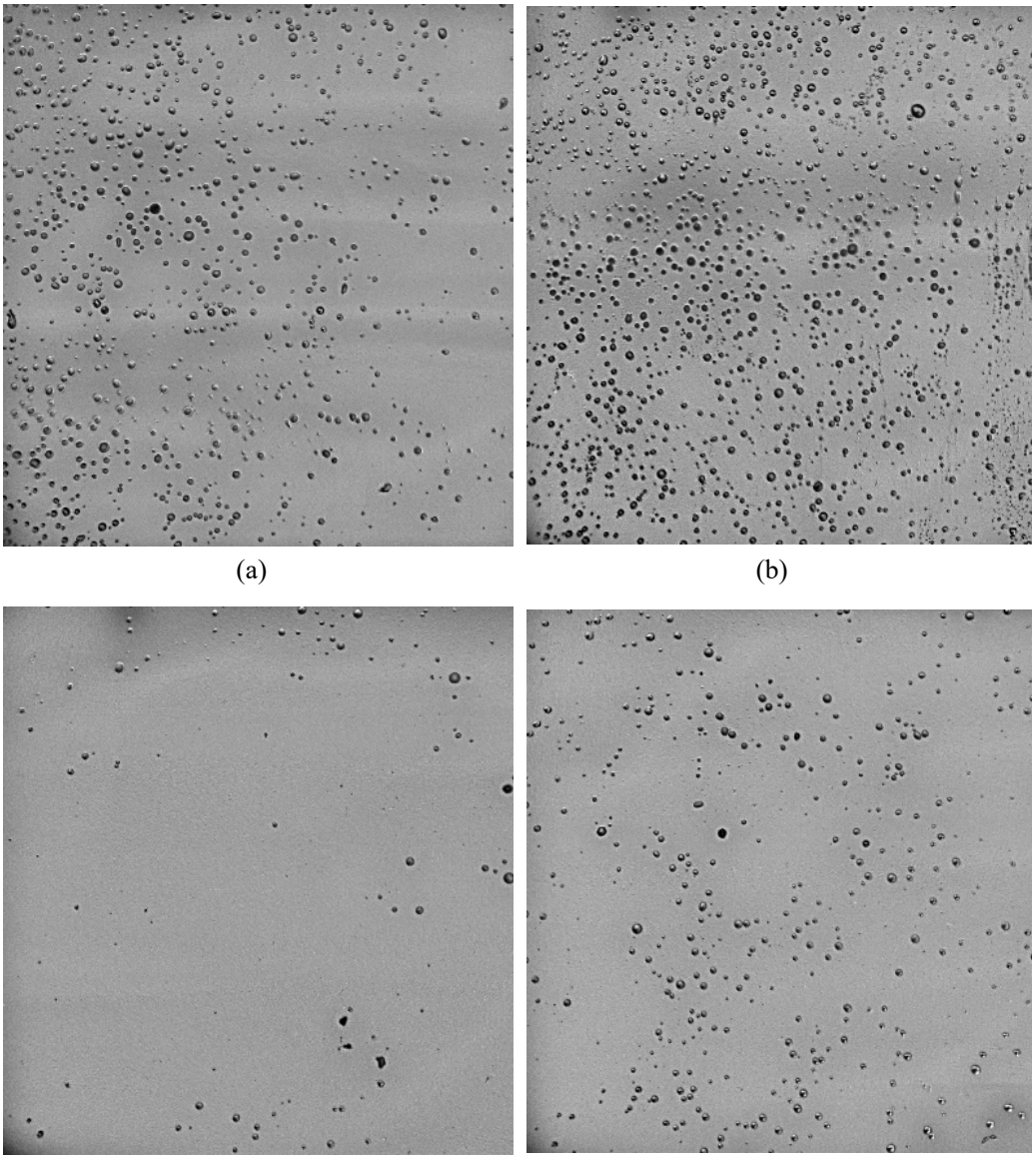

(a) (b)

(c) (d)

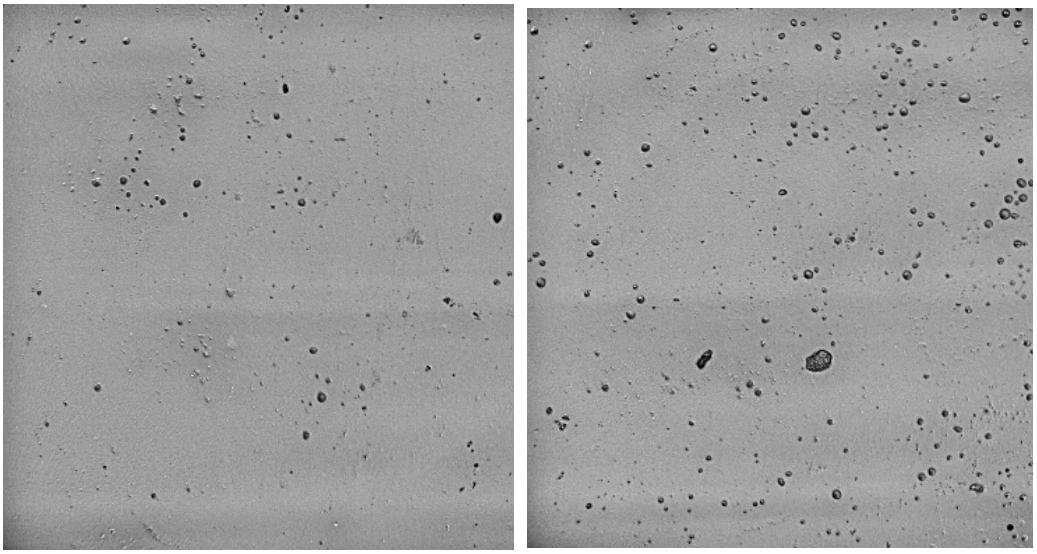

(e) (f)

Figure S6 Photos after 2.5 μm particle deposition for the semi-circular height of 2000 μm: (a) p/e=3 (b) p/e=4 (c) p/e=5, upstream (d) p/e=5, downstream (e) p/e=6, upstream (f) p/e=6, downstream

Table S2. Non-dimensional deposition velocity at different locations in the cavity for the particle size of 0.5 μm

Height (μm)	p/e=3	p/e=4	p/e=5	p/e=6	p/e=10
2000	1.35×10^{-4}	2.89×10^{-4}	Upstream (6.79×10^{-4}): Downstream (1.67×10^{-3}) =1:2.46	Upstream (3.04×10^{-4}): Downstream (1.42×10^{-3}) =1:4.67	
500	9.3×10^{-5}	6.86×10^{-4}	Upstream (6.77×10^{-4}): Downstream (1.17×10^{-3}) =1:1.73	Upstream (9.0×10^{-4}): Downstream (1.95×10^{-3}) =1:2.16	Upstream (3.43×10^{-4}): Center (4.74×10^{-4}): Downstream (8.88×10^{-4}) =1:1.38:2.59

Table S3. Non-dimensional deposition velocity at different locations in the cavity for the particle size of 2.5 μm

Height (μm)	p/e=3	p/e=4	p/e=5	p/e=6
2000	3.46×10^{-2}	3.79×10^{-2}	Upstream (5.63×10^{-3}): Downstream (1.53×10^{-2}) =1:2.72	Upstream (4.74×10^{-3}): Downstream (1.69×10^{-2}) =1:3.57

500	6.49×10^{-4}	6.59×10^{-3}	Upstream (4.70×10^{-3}): Downstream (1.97×10^{-2}) =1:4.19	Upstream (3.50×10^{-3}): Downstream (1.56×10^{-2}) =1:4.46

S3. FLOW PATTERNS AT THE LEEWARD AND WINDWARD SIDES OF THE CAVITY

The flow field for different heights of semi-circular patterned surface is similar. In this section the *p/e* value of 5, 6 and 10 with the semi-circular height of 2000 μm is discussed. At the *p/e* value of 3 and 4, a recirculation flow exists for different heights of semi-circular patterned surface. Based on the flow fields at the *p/e* value of 5 and 6 (Figure S7), the recirculation flow is found at the leeward side of the upward semi-circular rib and the separation region appears at the windward side of the downward semi-circular rib. For the case of p/e=10 at the semi-circular height of 2000 μm, three different locations can be defined from Figure S8 (a). X-direction wall shear stress was used to find out the area-weighted percentage of upstream, center and downstream locations in Figure S8(b). The area percentage of upstream, center and downstream was indicated by the changing of the shear stress symbol (from negative to positive or from positive to negative). In Figure S8(b), the upstream region (negative values of shear stress) represents the reattachment length in Figure S8(a). The center region (positive values) represents the separation length, and the downstream region (negative values) represents a spiral flow which has the same direction as the recirculation flow. The variation of x-direction wall shear stress can also be used to calculate the area-weighted percentage for different heights of a semi-circular patterned surface. Table S4 concluded the area-weighted ratio under each *p/e* value for the semi-circular height of 2000 μm. The area-weighted percentage for different locations in Table S4 is applicable to all heights of semi-circular patterned surface. l_u, l_c and l_d

represent the length of upstream, center and downstream regions. It can be observed that the percentage of recirculation length gradually decreases as the p/e value increases. However, the area percentage of the center region increases.

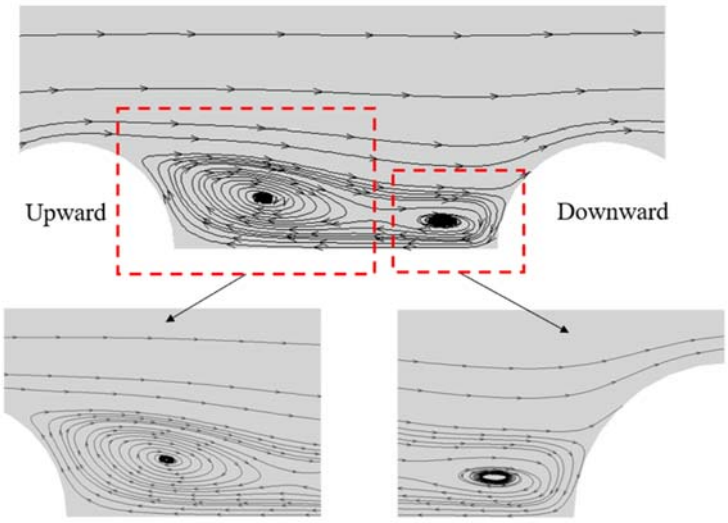

(a)

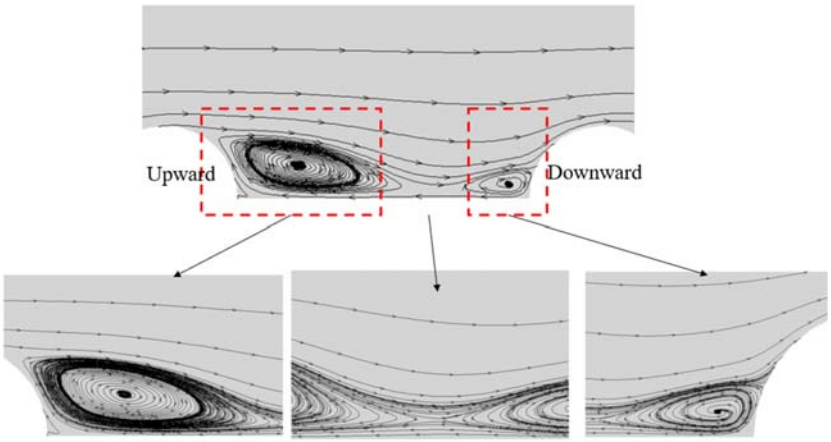

(b)

Figure S7. Flow pattern for 2000 µm semi-circular at (a) p/e of 5 (b) p/e of 6

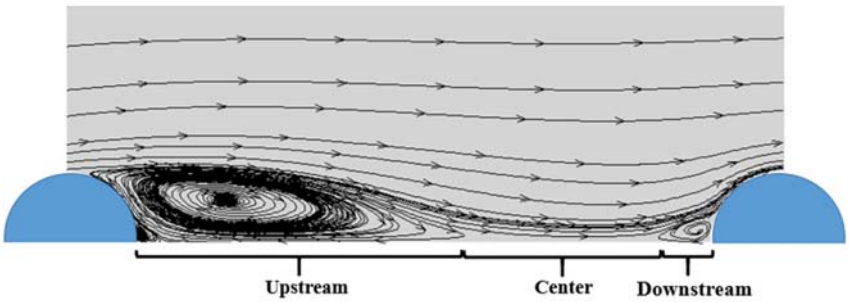

(a)

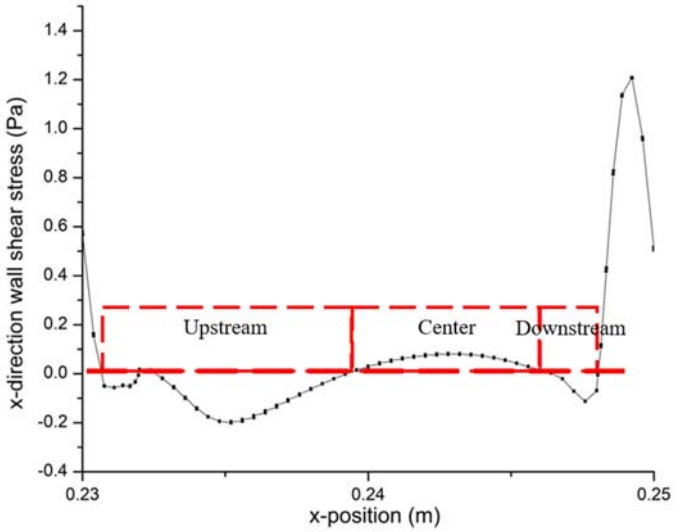

(b)

Figure S8 Illustration of different deposition locations for the semi-circular height of 2000 µm at a *p/e* of 10: (a) velocity vector field between the cavity (b) x-direction wall shear stress (Pa) between the cavity

Table S4 Area-weighted ratio for all heights of semi-circular patterned surface under each *p/e*

p/e=3	p/e=4	p/e=5	p/e=6	p/e=10
l_u=*e*	l_u=*2e*	l_u: l_d=*2.1e:0.9e*	l_u: l_d =*2.4e:1.6e*	l_u: l_c: l_d =*4e:3.2e:0.8e*

Figure S9 displays the pressure drop (*Pa*) along the channel for different heights of semi-circular patterns. The pressure drop increases from *p/e* value of 3 to 6 at the semi-circular heights of 2000 µm, 1500 µm and 800 µm. With a *p/e* value of 3, the flow was not easily separated into the cavity and the pressure drop is mainly due to the obstructions by the semi-circular ribs. The smaller the semi-circular height decreases, the more the pressure drop suffers

along the channel. At the *p/e* value of 6, the flow separates after it encounters the semi-circular ribs. The flow resistance increased as the path of flow becomes more complicated compared with the straightforward flow field in a smooth channel. With the *p/e* value at 10 and 15, the pressure drop decreased because there are not many flow separations for the fluid to turn around. Understanding the pressure drop at different *p/e* value will help to decrease the energy consumption, as well as enhance the efficiency of the current ventilation ducting system.

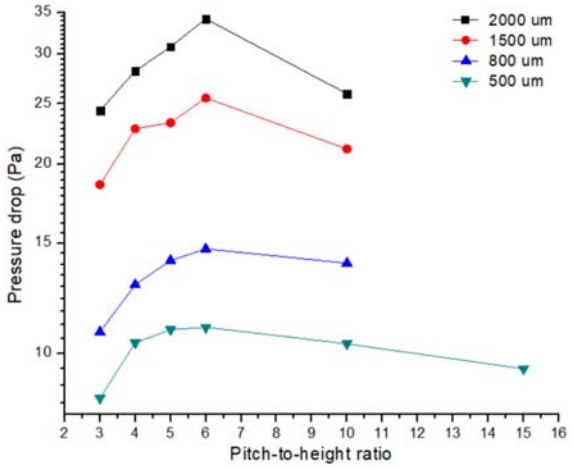

Figure S9 Pressure drop (Pa) for different heights of semi-circular patterns

References

Hinds, W. C. (2012). *Aerosol technology: Properties, behavior, and measurement of airborne particles*. 2nd ed. John Wiley & Sons.

Lai, A. C., Byrne, M. A. and Goddard, A. J. (2000). Enhanced particle loss in ventilation duct with ribbed surface. *Building and Environment* 35:425-432.